

Star cluster formation and cloud dispersal by radiative feedback: dependence on metallicity and compactness

Hajime Fukushima^{1*}, Hidenobu Yajima¹, Kazuyuki Sugimura², Takashi Hosokawa³, Kazuyuki Omukai⁴ and Tomoaki Matsumoto⁵

¹Center for Computational Sciences, University of Tsukuba, Ten-nodai, 1-1-1 Tsukuba, Ibaraki 305-8577, Japan

²Department of Astronomy, University of Maryland, College Park, MD 20740, USA

³Department of Physics, Graduate School of Science, Kyoto University, Sakyo, Kyoto 606-8502, Japan

⁴Astronomical Institute, Graduate School of Science, Tohoku University, Aoba, Sendai 980-8578, Japan

⁵Faculty of Sustainability Studies, Hosei University, Fujimi, Chiyoda, Tokyo 102-8160, Japan

Accepted XXX. Received YYY; in original form ZZZ

ABSTRACT

We study star cluster formation in various environments with different metallicities and column densities by performing a suite of three-dimensional radiation hydrodynamics simulations. We find that the photoionization feedback from massive stars controls the star formation efficiency (SFE) in a star-forming cloud, and its impact sensitively depends on the gas metallicity Z and initial cloud surface density Σ . At $Z = 1 Z_{\odot}$, for instance, the SFE increases from 0.02 to 0.3 with Σ from 10 to 300 $M_{\odot}\text{pc}^{-2}$. In low-metallicity cases $10^{-2} - 10^{-1} Z_{\odot}$, star clusters form from atomic warm gases because the molecule formation time is not short enough with respect to the cooling or dynamical time. In addition, the whole cloud is disrupted more easily by expanding HII bubbles which have higher temperature owing to less efficient cooling. With smaller dust attenuation, the ionizing radiation feedback from nearby massive stars is stronger and terminate star formation in dense clumps. These effects result in inefficient star formation in low-metallicity environments: the SFE is reduced by a factor of ~ 0.3 for the cases with $Z = 10^{-2} Z_{\odot}$ regardless of Σ . Newborn star clusters are also gravitationally less bound. We further develop a new semi-analytical model that can reproduce the simulation results well, particularly the observed dependencies of the SFEs on the cloud surface densities and metallicities.

Key words:

1 INTRODUCTION

The formation of massive stars is an essential factor in understanding the cosmic star formation history (Madau & Dickinson 2014) and galactic dynamics (Pillepich et al. 2018). Stellar feedback from them regulates the total star formation rate within a galaxy (e.g., Schaye et al. 2010; Wise et al. 2012; Hasegawa & Semelin 2013; Yajima et al. 2017) and induce galactic outflow (e.g., Heckman et al. 1990, 2015). Ionizing radiation from them destroys parent clouds and leaks out to the interstellar and intergalactic space (Kim et al. 2019; He et al. 2020). Most massive stars are known to be born as members of clusters. However, the formation mechanism of the star clusters has not been fully understood yet.

The star formation efficiency (SFE) is a pivotal quantity

in the star-cluster formation as it determines whether a newborn cluster remains gravitationally bound after the cloud dispersal. As suggested by observations of nearby galaxies, the star formation in the entire galaxy proceeds slowly with the depletion timescale ~ 1 Gyr (e.g. Kennicutt 1998; Bigiel et al. 2008; Momose et al. 2013). On the other hand, the star formation in an individual giant molecular cloud (GMC) only lasts for ~ 10 Myr (Hartmann et al. 2001; Fukui & Kawamura 2010) by considering observed numbers of GMCs in local galaxies (e.g., Chevance et al. 2020). This implies that only a small fraction of the molecular gas is converted into stars and the rest returns into an interstellar or intergalactic medium. Recently, Kruijssen et al. (2019) showed that the lifetime of GMCs are about one dynamical time, and the SFE is only a few percents, by analyzing the spatial de-correlation between young stars and star-forming regions in the spiral galaxy NGC300. They indicated that GMCs are disrupted before the end of the lifetimes of OB stars,

* E-mail: fukushima@ccs.tsukuba.ac.jp

and thus pre-supernova feedback, such as ultraviolet (UV) radiation feedback or stellar winds, regulated star formation in GMCs.

Extreme ultraviolet (EUV; $13.6 \text{ eV} \leq h\nu \lesssim 1 \text{ keV}$) radiation from massive stars creates HII bubbles and heat up the gas to $\sim 10^4 \text{ K}$. The HII bubbles expand rapidly because of the high thermal pressure so that heated materials are photoevaporated against the gravitational pull from the gas and stars. Based on simple analytical models, previous studies suggested that the radiative feedback suppresses star formation in GMCs, resulting in the low SFEs (e.g., Williams & McKee 1997; Matzner 2002; Krumholz et al. 2006; Kim et al. 2016). Fall et al. (2010) derived an analytical expression for the SFE as a function of the surface density of the clouds. In reality, however, the supersonic turbulent motion shapes hierarchical cloud structures. HII regions forming around newborn clusters expand across such complex structures and finally destroy the GMCs.

Numerical simulations have been utilized (e.g., Vázquez-Semadeni et al. 2010; Dale et al. 2012) to investigate the star cluster formation and cloud dispersal through the realistic evolution. Geen et al. (2017) showed the disruption of molecular clouds due to the radiative feedback by using radiation hydrodynamics (RHD) simulations with a diffuse approximation for the radiative transfer (RAMSES-RT; Rosdahl et al. 2013). They showed that the radiative feedback quenches the star formation immediately, and the SFE increases with increasing cloud column density. Using the same simulation code, He et al. (2019) investigated this problem in a wider parameter range of initial gas clouds and showed that the massive-end slope of simulated sink mass function was similar to that of Salpeter-like initial mass function.

Recently, Kim et al. (2018) showed the cloud dispersal occurred within 2-10 Myr after the onset of radiative feedback using the RHD simulations with a ray-tracing scheme. They found a close relationship between the SFEs and the surface densities of gas clouds. However, their simulations were limited to the clouds with metallicity $Z = 1 Z_{\odot}$. Varying the metallicity potentially changes the star formation and feedback processes. For instance, a smaller amount of dust grains results in less attenuation of the stellar UV radiation, which strengthens the feedback effect (e.g., Fukushima et al. 2020).

In this paper, we study the star-cluster formation and resulting cloud dispersal for various cases with metallicities $Z = 10^{-2} - 1 Z_{\odot}$. We perform three-dimensional RHD simulations with SFUMATO-RT (Sugimura et al. 2020), an Eulerian adaptive mesh refinement (AMR) hydrodynamics code (Matsumoto 2007) coupled with the radiative transfer solver using the ray-tracing method. Also, we calculate the gas temperature considering metal and dust cooling, while Kim et al. (2018) assumed the temperature with an approximation based on local ionization degree. The temperature of ionized gas decreases as the metallicity increases due to the metal-line cooling, e.g., OII and OIII (Osterbrock & Ferland 2006). As discussed in He et al. (2019), an HII bubble expands earlier at lower metallicities, resulting in the shorter lifetime of the clouds.

In the current work, we consistently solve the thermal and chemical states of the neutral and molecular gases, from which stars form. With $Z \gtrsim 10^{-2} Z_{\odot}$, CO molecules

($n_{\text{H}} < 10^5 \text{ cm}^{-3}$) and dust grains ($n_{\text{H}} > 10^5 \text{ cm}^{-3}$) are efficient coolant for the molecular gas (e.g., Omukai et al. 2005), with which the temperature could drop to the CMB value. The atomic gas also cools mainly via OI and CII fine-structure line emission. Far-ultraviolet (FUV; $6.0 \text{ eV} \leq h\nu \leq 13.6 \text{ eV}$) photons are the dominant heating sources for the neutral gas via the photodissociation of hydrogen molecules and photoelectric heating of dust grains. As a result, the HII bubbles are surrounded by a warm neutral layer where the temperature is raised up to a few 100 K in the case of $Z = Z_{\odot}$ (so-called the photodissociation region or PDR; e.g., Hollenbach & Tielens 1999; Hosokawa & Inutsuka 2005, 2006). Our simulations show that at very low metallicity of $Z = 10^{-2} Z_{\odot}$ the whole star-forming clouds are mostly dominated by such warm atomic gases, and that massive star clusters directly form from the atomic clouds.

We organize the rest of the paper as follows. In Section 2, we describe the numerical method and setup of our simulations. We present our simulation results in Section 3. We then develop a semi-analytical model that helps us to interpret numerical results in Section 4. Section 5 is for summary and discussions. We describe the details of the numerical simulations and the fitting formula of the fraction of hydrogen ionization in an HII region in Appendix A and B.

2 NUMERICAL METHOD

We perform RHD simulations with SFUMATO-RT (Sugimura et al. 2020), a modified version of the self-gravitational magnetohydrodynamics code with AMR, SFUMATO (Matsumoto 2007; Matsumoto et al. 2015). SFUMATO-RT has been developed to solve radiative transfer with the adaptive ray-tracing method (Abel & Wandelt 2002) and non-equilibrium chemistry of the primordial gas. For the current purpose, we further add the effects of heavy elements (e.g., dust grains, atomic carbon, oxygen, etc.) as described in Section 2.1.

The hydrodynamics is solved with the Cartesian coordinates. We initially set uniform 64 meshes in each direction and refine them during the simulations as the gas density gradually increases according to the refinement criterion of at least 5 meshes for one Jeans length. The computational box at the coarsest grid level is large enough to cover the whole cloud, $-2R_{\text{cl}} \leq x \leq 2R_{\text{cl}}$ on a side, where R_{cl} is the cloud radius and the origin of coordinates (x, y, z) is at the box center. We set the maximum level of the refinement so that the maximum resolution becomes 0.078 pc regardless of the box size. In the case with the maximum level $l_{\text{max}} = 5$, the effective resolution corresponds to $64 \times 2^5 = 2048$ uniform meshes on a side. We solve the following set of equations for compressible hydrodynamics:

$$\frac{\partial \rho}{\partial t} + \nabla \cdot (\rho \mathbf{v}) = 0, \quad (1)$$

$$\frac{\partial (\rho \mathbf{v})}{\partial t} + \nabla \cdot (\rho \mathbf{v} \otimes \mathbf{v}) + \nabla P = \rho (\mathbf{g} + \mathbf{f}), \quad (2)$$

$$\frac{\partial (\rho E)}{\partial t} + \nabla \cdot [(\rho E + P) \mathbf{v}] = \rho (\mathbf{g} + \mathbf{f}) \cdot \mathbf{v} + \Gamma - \Lambda, \quad (3)$$

$$E = \frac{|\mathbf{v}|^2}{2} + (\gamma - 1)^{-1} \frac{P}{\rho}, \quad (4)$$

where ρ , P , \mathbf{v} , \mathbf{g} , E , Γ and Λ are the density, pressure, velocity, gravitational force, total energy, the heating and cooling functions. In Equation (2) and (3), \mathbf{f} is the radiation forces per unit mass. We consider the absorption of ionizing photons by HI and dust grains, and that of non-ionizing photons by dust grains. We also calculate the specific heat γ as a function of temperature and chemical abundances (Omukai & Nishi 1998). In this study, we include thermal processes due to heavy elements in addition to those in the primordial gas.

2.1 Chemical and thermal processes

We update the chemistry module of SFUMATO-RT to calculate the chemical and thermal evolution of the gas. We consider the chemical network of 11 species: H, H₂, H⁻, H⁺, H₂⁺, e, CO, CII, OI, OII and OIII. To follow the CO formation, we adopt the simple chemical network of Nelson & Langer (1997). In this model, we only explicitly include CII and CO as carbon species. CO is assumed to form via hydrocarbon radicals without CI in the chemical network. Glover & Clark (2012b) and Gong et al. (2017) showed limitations of such a simplified treatment and provided the alternative extended network. However, our qualitative results of the cluster formation and cloud dispersal do not rely on those details because CII becomes the dominant coolant instead of CO molecules (e.g., Glover & Clark 2012a). As in Fukushima et al. (2020), we assume that the neutral fraction of oxygen is the same as hydrogen and that OII and OIII are in the chemical equilibrium with photoionization and recombination. The metal-line cooling by OII and OIII becomes the dominant coolant in HII regions at metallicity as high as $Z = 1 Z_{\odot}$.

The total heating/cooling rates in Equation (3) are given as

$$\Gamma = \Gamma_{\text{prim}} + \Gamma_{\text{H}_2, \text{d}} + \Gamma_{\text{pe}}, \quad (5)$$

$$\Lambda = \Lambda_{\text{prim}} + \Lambda_{\text{d}} + \Lambda_{\text{m, line}}, \quad (6)$$

where Γ_{prim} and Λ_{prim} are the thermal processes related to primordial star formation as in Hosokawa et al. (2016). In this study, we newly add heating of H₂ formation on dust grains ($\Gamma_{\text{H}_2, \text{d}}$) and energy transport between dust grains and gas (Λ_{d}) as in Fukushima et al. (2020). In Equation (5), Γ_{pe} is the photoelectric heating rate, and we describe its details in Appendix A. We consider CII, CO, OI, OII and OIII as the metal-line cooling ($\Lambda_{\text{m, line}}$). To calculate the cooling rates of CII, OI, OII, and OIII, we solve the statistical equilibrium of each energy level as in Fukushima et al. (2020). For the cooling rate of CO rotational transitions, we use the fitting function by Omukai et al. (2010). We assume that the dust-to-gas mass ratio is 0.01 at $Z = 1 Z_{\odot}$ and decreases linearly in proportion to the metallicity. We adopt the MRN mixture (Mathis et al. 1977) for the grain size distribution.

The radiative processes considered in our simulations are photoionization of HI and OII, photodissociation of H₂ and CO, and photoelectric heating of dust grains. We allow that the gas and dust have different temperatures due to the ineffective coupling. The dust temperature is calculated from the energy balance between the energy exchange with gas and absorption/emission of radiation. We also consider the radiation pressure via the direct stellar photons (\mathbf{f} in Eq.

2 and 3). The optical depth of a star-forming cloud for dust thermal radiation is estimated as

$$\tau_{\text{IR}} = \rho R_{\text{cl}} \kappa_{\text{IR}} = 6.3 \times 10^{-2} \left(\frac{\Sigma}{80 M_{\odot} \text{pc}^{-2}} \right) \left(\frac{Z}{Z_{\odot}} \right), \quad (7)$$

where R_{cl} and Σ are the radius and surface density of the cloud. Here, we use the opacity for thermal emission as $\kappa_{\text{IR}} = 5 \text{ cm}^2 \text{ g}^{-1} (Z/Z_{\odot})$. Star-forming clouds examined in this study are optically thin for dust thermal emission. Thus we ignore the radiation pressure of dust thermal emission, although it can be significant in clouds more compact than those examined in this paper (e.g., Murray et al. 2010). We describe the method of radiative transfer in more detail in Appendix A.

We set the temperature floor at $T = 10 \text{ K}$ in our simulations, supposing the CMB temperature at the redshift $z \approx 2.5$. This floor does not affect our results because the gas temperature is normally much higher than the floor value, particularly in low-metallicity cases. We do not consider stellar UV background radiation, which would permeate into the cloud externally. We discuss this effect later in Section 4.1.

2.2 Sink particles and radiation sources

We employ the sink particle technique to follow long-term evolution without resolving very dense structures by adding finer grid refinement levels. We insert a sink particle in a mesh that satisfies the following conditions (Federrath et al. 2010; Matsumoto et al. 2015): 1) the gas density is above the threshold value, 2) the gravitational potential is a local minimum, 3) the velocity divergence $\nabla \cdot \mathbf{v}$ and all the eigenvalues of the velocity gradient tensor $\nabla \mathbf{v}$ are negative and 4) the sum of the thermal, kinetic and gravitational energies inside the sink radius is negative ($E_{\text{th}} + E_{\text{kin}} + E_{\text{gr}} < 0$). We determine the density threshold in a way proposed by Gong & Ostriker (2013), as in Kim et al. (2018). Assuming the density profile of Larson-Penston solution (Larson 1969; Penston 1969) around the density peak, we set the density threshold as $\rho_{\text{thr}} = 8.86 c_s^2 / (\pi G \Delta x^2) = 5.34 \times 10^{-19} \text{ g cm}^{-3}$, where Δx is the minimum mesh size and c_s is the sound speed of gas with temperature $T = 20 \text{ K}$. In practice, if the gas temperature is higher than 20K, the condition (4) of the sink creation is not satisfied at ρ_{thr} and the gas density becomes higher than ρ_{thr} until all of the conditions are fulfilled. Therefore, the threshold density ρ_{thr} should be regarded as the lower limit for the sink creation. We set the sink radius $r_{\text{sink}} = 2\Delta x$ and merge nearby sink particles if their separation distances are smaller than $2r_{\text{sink}}$. The velocity of the merged sink particles is determined from momentum conservation.

We regard each sink particle as a star cluster, as we cannot resolve individual stars due to high computational cost, and calculate the transfer of radiation emitted from each cluster particle. To evaluate the luminosity and spectrum of the star cluster, we take the average of the stellar isochrone given by Chen et al. (2015), where the Chabrier IMF (Chabrier 2003) with a stellar-mass range from $0.1 M_{\odot}$ to $150 M_{\odot}$ is used. In our simulations, the duration time of star formation is on the order of Myr, and thus we use their isochrone at $t = 1 \text{ Myr}$. We assume that low-mass cluster particles with $< 50 M_{\odot}$ do not emit ionizing photons, neglecting the weak contributions from the smaller clusters.

Table 1. Models considered

model	$M_{\text{cl}} [M_{\odot}]$	$R_{\text{cl}} [\text{pc}]$	$Z [Z_{\odot}]$	$n_{\text{ini}} [\text{cm}^{-3}]$	$\Sigma [M_{\odot} \text{pc}^{-2}]$	$\sigma_0 [\text{kms}^{-1}]$	$t_{\text{ff}} [\text{Myr}]$	l_{max}	Feedback
M4R10Z0	10^4	10	1	70	32	1.1	5.2	3	PI ^a , RP ^b
M4R20Z0	10^4	20	1	8.7	8	0.80	15	4	PI, RP
M5R10Z0	10^5	10	1	700	320	3.6	1.7	3	PI, RP
M5R20Z0	10^5	20	1	87	80	2.5	4.7	4	PI, RP
M5R40Z0	10^5	40	1	11	20	1.8	13	5	PI, RP
M4R10Z-1	10^4	10	10^{-1}	70	32	1.1	5.2	3	PI, RP
M4R20Z-1	10^4	20	10^{-1}	8.7	8	0.80	15	4	PI, RP
M5R10Z-1	10^5	10	10^{-1}	700	320	3.6	1.7	3	PI, RP
M5R20Z-1	10^5	20	10^{-1}	87	80	2.5	4.7	4	PI, RP
M5R40Z-1	10^5	40	10^{-1}	11	20	1.8	13	5	PI, RP
M4R10Z-2	10^4	10	10^{-2}	70	32	1.1	5.2	3	PI, RP
M4R20Z-2	10^4	20	10^{-2}	8.7	8	0.80	15	4	PI, RP
M5R10Z-2	10^5	10	10^{-2}	700	320	3.6	1.7	3	PI, RP
M5R20Z-2	10^5	20	10^{-2}	87	80	2.5	4.7	4	PI, RP
M5R40Z-2	10^5	40	10^{-2}	11	20	1.8	13	5	PI, RP
M5R20Z0PI	10^5	20	1	87	80	2.5	4.7	4	PI
M5R20Z0RP	10^5	20	1	87	80	2.5	4.7	4	RP

Notes. Column 1: model names, Column 2: cloud masses, Column 3: cloud radii, Column 4: metallicities, Column 5: initial number densities, Column 6: surface densities, Column 7: three-dimensional velocity dispersions, Column 8: free fall times, Column 9: maximum refinement levels

^a“PI” represents photoionization feedback

^b“RP” represents radiation-pressure feedback

This is a reasonable approximation as the expected number of massive stars ($\gtrsim 10 M_{\odot}$) is less than unity for such small clusters. With this procedure, we significantly reduce the computational costs of solving radiation transfer.

2.3 Initial conditions

Table 1 summarizes the models considered in this paper. We set uniform density spheres with turbulent velocities as the initial conditions. We consider five different clouds with masses $M_{\text{cl}} = 10^4$ and $10^5 M_{\odot}$ and size $R_{\text{cl}} = 10\text{--}40$ pc, which are consistent with the observed properties of galactic and extragalactic GMCs (e.g., [Faesi et al. 2018](#)). The gas metallicity is assumed to be the solar value in the fiducial model, but we also consider lower-metallicity environments with 10^{-2} and $10^{-1} Z_{\odot}$. To see the impact of the individual feedback effect, we also simulate the cases where we only consider either photoionization (M5R20Z0PI) or radiation pressure induced by dust grains (M5R20Z0RP) for a star-forming cloud with $(M_{\text{cl}}, R_{\text{cl}}, Z) = (10^5 M_{\odot}, 20\text{pc}, 1Z_{\odot})$. We set the initial gas temperature of 20 K irrespective of metallicity, which is the approximate value of collapsing clouds when the central density reaches $n_{\text{ini}} \sim 10\text{--}10^3 \text{ cm}^{-3}$ ([Omukai et al. 2005](#)), the initial values in our simulations. Note, however, that the initial turbulent velocity is supersonic, as we will describe below, and thus the dynamics of the clouds are almost independent of the initial gas temperature. We also assume the atomic gas at the initial state. We set the abundance of hydrogen molecules is $y_{\text{H}_2} = 10^{-3}$ ¹, and other species are in atomic states. This assumption is motivated by theoretical prediction for low-metallicity star-forming regions ([Krumholz 2012](#)). On the other hand, observations show

¹ The abundance of species i is given as y_i ; that is the ratio of the number density of the species i to that of atomic hydrogen.

that the star-forming clouds are almost fully molecular at $Z = 1 Z_{\odot}$. In our simulations, molecules rapidly form in high-density parts within the clouds before the first cluster particle appears. The star formation then mostly occurs in the molecular clouds surrounded by rarefied atomic envelope. We also show that this is not necessarily the case for lower metallicity cases, where star clusters are formed in almost atomic clouds.

The supersonic turbulent velocity fields are added at the beginning of the simulations. As in the previous studies (e.g., [Matsumoto et al. 2015](#); [Kim et al. 2018](#)), we assume the velocity power spectrum of $P(k) \propto k^{-4}$ with wavenumber k , which corresponds to the velocity dispersion law of $\sigma(l) \propto l^{1/2}$ with length scale l ([Larson 1981](#)). The amplitude is given by setting the virial parameter

$$\alpha_0 = \frac{5\sigma_0^2 R_{\text{cl}}}{3GM_{\text{cl}}} \quad (8)$$

to be 0.5, where σ_0 is the three-dimensional velocity dispersion. We impose the same random turbulent fields in all models. The strength of the turbulent motions used in our simulations is comparable to that considered in [He et al. \(2019\)](#) ($\alpha = 0.4$). Note that [Kim et al. \(2018\)](#) adopted a larger value of $\alpha = 2.0$, i.e., the clouds less gravitationally unstable with stronger turbulence support.

3 RESULTS

We describe the results of our simulations in this section. In Section 3.1, we show the time evolution of the cloud being destroyed by the radiative feedback from a newborn star cluster, first for the fiducial solar-metallicity model and then for the low-metallicity model with $Z = 10^{-2} Z_{\odot}$ (models M5R20Z0 and M5R20Z-2 in Table 1). In Section 3.2, we

present the dependences of the SFEs and the timescale until star formation ceases on the cloud surface density and metallicity, obtained from all the examined cases. In Section 3.3, we show the time evolution of the half-mass radius and the mass distribution of star cluster particles to investigate the metallicity dependence of the gravitational boundness of the newborn clusters.

3.1 Star cluster formation and cloud dispersal

3.1.1 Fiducial solar-metallicity model

We first present the case with $(M_{\text{cl}}, R_{\text{cl}}, Z) = (10^5 M_{\odot}, 20 \text{ pc}, 1 Z_{\odot})$ as the fiducial model, which has the moderate initial cloud surface density $\Sigma \approx 80 M_{\odot} \text{ pc}^{-2}$ (see M5R20Z0 in Table 1). Figure 1 shows the evolution of the surface density Σ , temperature T on the xy -plane of $z = 0$, the column densities of H_2 (N_{H_2}) and CO (N_{CO}). In Figure 2, we show the volume rendering of the number density, together with the positions of star cluster particles and ionization front at the same snapshots as in Figure 1.

Early on, the turbulent motions and self-gravity control the evolution of the cloud. Sheet-like structures are induced by turbulent motions. At the intersection of these sheets, filamentary density structures appear. Then, the gas density gradually increases along the filaments due to self-gravity. At this time, the gas temperature is generally less than 30 K because of the cooling by heavy elements (CII, OI, and CO). The first star-cluster particle forms in the central region of the cloud when the elapsed time of the simulation is 3.8 Myr (Fig1-1, 2-1). After that, stars continuously form along the filaments in the central 10 pc region of the cloud, as shown in the snapshot at 4.7 Myr, which is equal to one free-fall time of the cloud, t_{ff} (Fig1-2, 2-2). Ionizing photons emitted by the stars begin to form HII regions, which expand outward due to enhanced thermal pressure of the ionized gas with $8000 - 10^4$ K. The ionization fronts propagate in gap regions between the filament structures since HII regions expand more quickly at lower densities. The filamentary structures are not disrupted by photoionization, but the expansion of HII regions starts to push them out (5.7 Myr, Fig1-3, 2-3). Finally, most of them are swept out and the star formation is quenched at 6.7 Myr (Fig1-4, 2-4). Even though the total emissivity of ionizing photons is large enough to completely ionize all the gas in the initial homogeneous cloud, HII regions cannot spread to the entire domains, and some filamentary structures survive until the final time of the simulation.

As the collapse of the cloud proceeds, H_2 and CO molecules gradually form in dense regions. In the snapshots at 3.9 Myr and 4.7 Myr of Figure 1, H_2 and CO molecules form in the entire region of the cloud. These molecules, however, cannot survive except in dense structures after FUV photons from stars begin to photodissociate them. Therefore, the column densities of H_2 and CO molecules only trace the dense filamentary structures in the snapshots at 5.7 Myr and 6.7 Myr of Figure 1.

The top panel of Figure 3 shows the time evolution of the mass in each component, i.e., the stars, neutral, molecular and ionized gases. Here, the neutral gas is defined as the neutral fraction of hydrogen is higher than 0.9. Hydrogen molecules form via the dust surface reaction, which increases

the amount of H_2 to 0.6 times the cloud mass at 4.5 Myr. After that, the stellar mass grows while the H_2 mass decreases due to the photodissociation by stellar FUV radiation. The ionized gas emerges as soon as the star formation begins, but its mass is kept small until it rapidly increases at 6.5 Myr as the HII regions expand and quench the star formation. At the final step of the simulation, clumps that contain the residual neutral component are being ionized gradually, without forming stars anymore within them.

In the above case, star formation starts at 3.8 Myr and is quenched at 6.7 Myr. Hence, the duration of the star formation (~ 3 Myr) is less than the free-fall time of the cloud (~ 4.7 Myr). The SFE defined by the final stellar mass normalized by the initial cloud mass is 19 percent. Kim et al. (2018) adopted a similar setup although they use $\alpha = 2.0$ (see Eq. 8) as the initial condition. The stronger turbulent field suppresses the star formation more effectively, but the resulting SFE is in the same order of 10 percent. He et al. (2019) adopted almost the same value of α and obtained the SFE value closer to ours, regardless of differences in the numerical methods such as the radiation transfer solver and the critical density of sink creation.

3.1.2 Low-metallicity model with $Z = 10^{-2} Z_{\odot}$

Next, we consider the low-metallicity case (M5R20Z-2 in Table 1) with $Z = 10^{-2} Z_{\odot}$ to examine the metallicity dependence of the evolution. Figures 4 and 5 illustrate the evolution for this case in the same styles as in Figures 1 and 2, respectively. In the early epoch, the turbulent motion gives the dominant contribution. The overall evolution looks similar to that in the fiducial case with $Z = 1 Z_{\odot}$ until the first star particle forms at 4.0 Myr (Fig 4-1, 5-1), even though the metal cooling is inefficient. Once star formation occurs, HII regions start to expand into low-density regions at 4.7 Myr (Fig 4-2, 5-2). Unlike the case with $Z = 1 Z_{\odot}$, dense filaments are easily photoionized, and they cannot survive around the HII region. The neutral gas is pushed out all at once, and star formation is completely quenched at 5.4 Myr (Fig 4-3, 5-3). Finally, the HII regions spread over the entire cloud and complete the photoevaporation of the gas inside the cloud at 5.7 Myr (Fig 4-4, 5-4).

Only small amounts of H_2 and CO molecules form along the filaments in the early phase of the cloud collapse, but the stellar FUV photons easily dissociate them. As shown in Figure 4, H_2 and CO molecules completely disappear after one free-fall time unlike for the cloud with $Z = 1 Z_{\odot}$ (see Fig 4-2). The cloud becomes dark in CO lines soon after the star formation begins.

In the bottom panel of Figure 3, we show the time evolution of the mass in each component for the case with $Z = 10^{-2} Z_{\odot}$. We see that the H_2 mass is much lower than that for the case with $Z = 1 Z_{\odot}$ throughout the evolution. Since H_2 formation on the dust grains is inefficient due to lower metallicity (and hence lower dust abundance), most of the gas remains atomic from the beginning of the simulation. In this case, the star cluster formation occurs in an almost atomic cloud rather than in a molecular cloud (Krumholz 2012). Meanwhile, the ionized gas mass increases until the ionized gas is finally evaporated from the cloud. The star formation stops at 5 Myr, with the duration of star formation ~ 1 Myr, much shorter than in the case with $Z = 1 Z_{\odot}$.

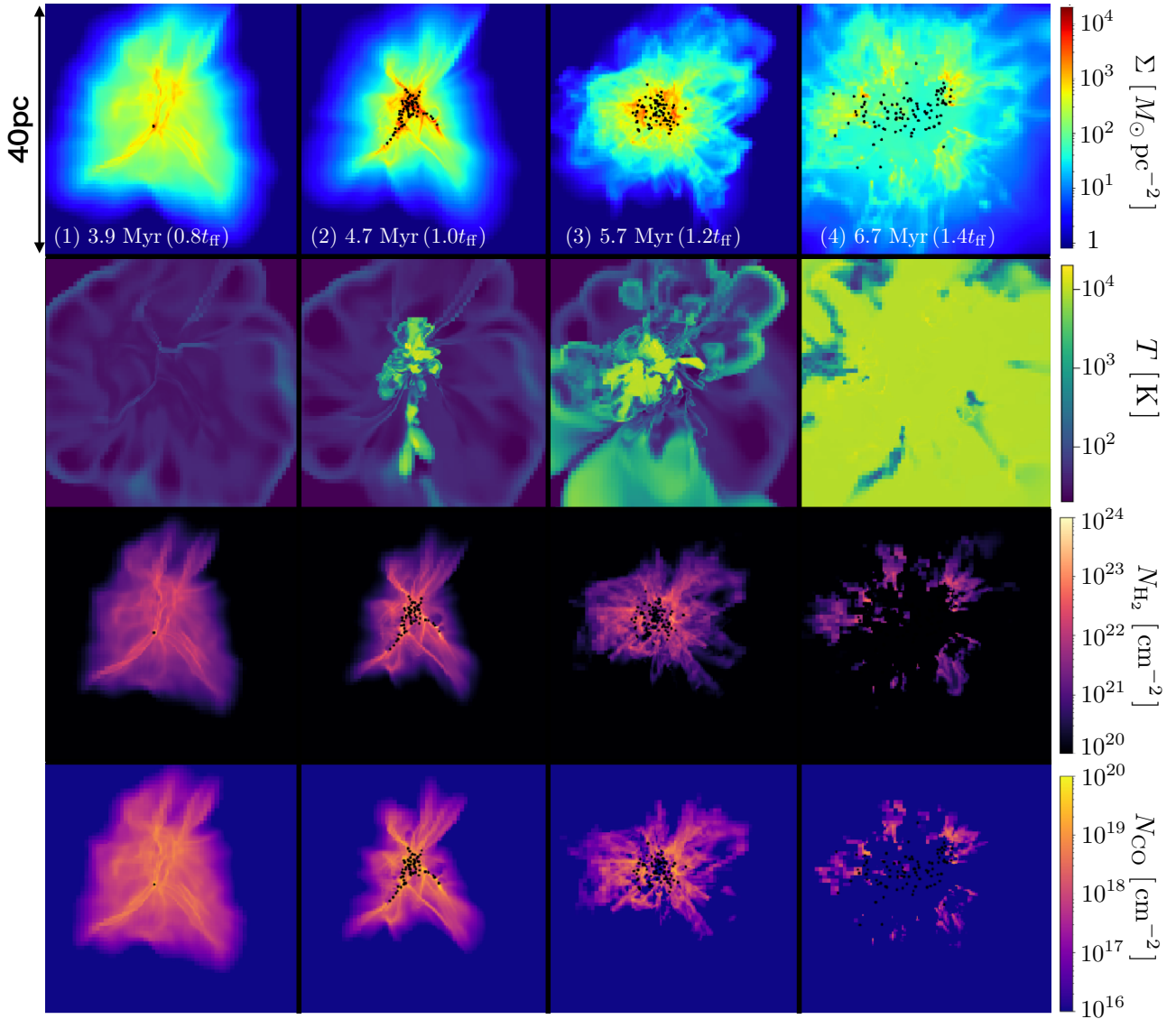


Figure 1. The cloud dispersal and formation of the star cluster for the fiducial model with $(M_{\text{cl}}, R_{\text{cl}}, Z) = (10^5 M_{\odot}, 20 \text{ pc}, 1Z_{\odot})$. We plot the surface density, temperature (on a slice) and the column densities of H_2 and CO molecules from top to bottom. The four panels at each row show the snapshots at the epochs of $t = 3.9, 4.7, 5.7$ and 6.3 Myr. The black dots represent the positions of the star cluster particles.

The SFE is 5 percent and smaller than that for $Z = 1 Z_{\odot}$ by a factor of ~ 3 . He et al. (2019) also performed one simulation run assuming $Z = 1/40 Z_{\odot}$, and they obtained a similar reduction rate of the SFE.

3.1.3 Radiation pressure on dust grains

In Section 3.1.1 and 3.1.2, we have seen that the expansion of HII regions quenches star formation while the radiation pressure on dust grains also affects the gas motion. Here, we investigate the individual effects of photoionization and radiation pressure on star formation separately. Figure 6 shows the time evolution of total stellar masses in the cases where we only consider either photoionization (M5R20Z0PI, dashed line) or radiation pressure (M5R20Z0RP, dot-dashed line). With only photoionization, star formation starts at

~ 4.5 Myr, and continues until ~ 7 Myr. The star formation history is almost the same as in the fiducial case, where we include both photoionization and radiation pressure effects. On the other hand, with only radiation pressure effect the SFE is very high exceeding 0.8. This result demonstrates that the photoionization feedback plays the leading role in regulating star formation. As given in Equation (8), the kinetic energy of turbulent motion is less than the gravitational binding energy in the initial condition. Then, the star clusters appear in the central region of the cloud, and the gas accretes onto the central star-forming regions in a spherical symmetric fashion, as shown in Figure 1. In such a situation, the supply of gas is suppressed if the momentum flux of radiation exceeds that of the inflow (Wolfire & Cassinelli

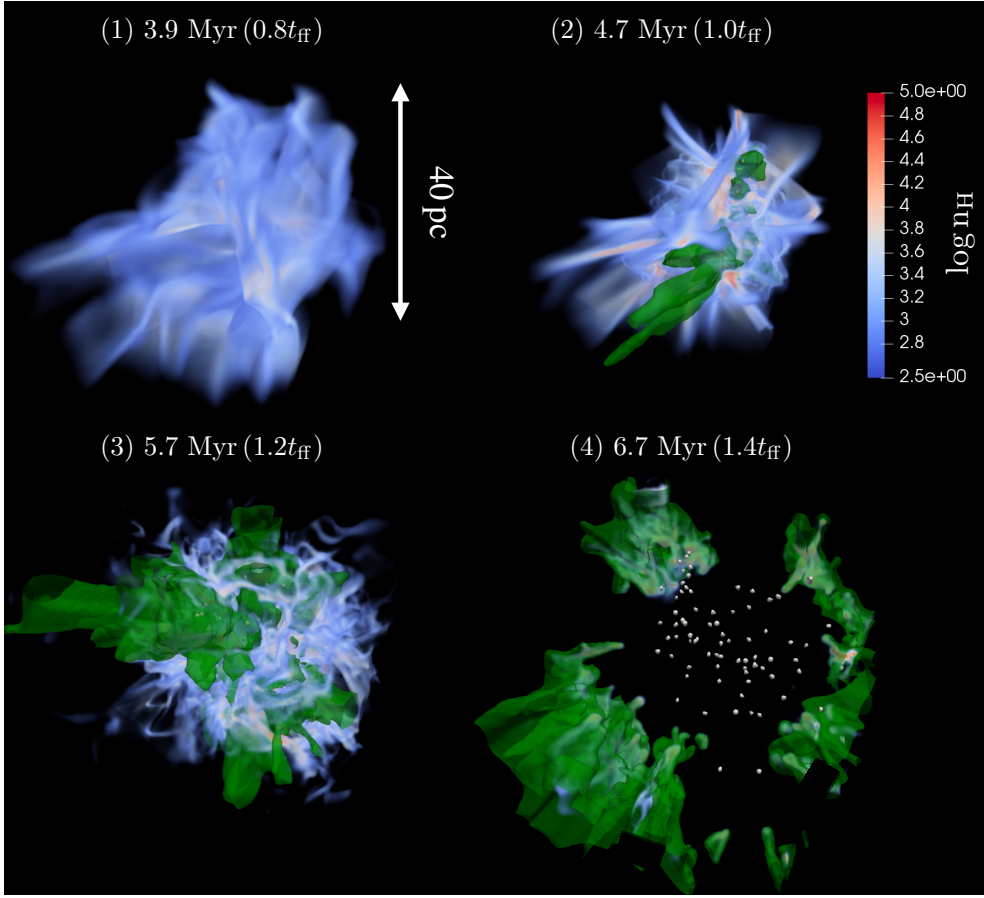


Figure 2. 3D volume rendering of the density field, together with the ionization fronts (green surface) where the ionization degree is 0.8, for the same case as in Figure 1 with $(M_{\text{cl}}, R_{\text{cl}}, Z) = (10^5 M_{\odot}, 20 \text{ pc}, 1 Z_{\odot})$. Each panel shows the snapshot at the same epochs as in Figure 1. The white dots in the panel (4) represent the positions of the star cluster particles. The box size is 40 pc on a side.

1987),

$$\frac{L_*}{4\pi R^2 c} > \rho u^2, \quad (9)$$

where L_* , R and u are total stellar luminosity, the distance from the star-forming region and the infall velocity of the gas. Here, we assume that the infall velocity to the star cluster is the free-fall velocity as $u = \sqrt{2GM_*/R}$ where M_* is the total stellar mass. Using the relation between the stellar mass and luminosity $L_* = l_* M_*$ where the factor of proportionality $l_* = 1.2 \times 10^3 L_{\odot} M_{\odot}^{-1}$ estimated in Section 2.2, Equation (9) becomes

$$R < \frac{l_*}{8\pi G c \mu n_{\text{H}}} = 0.65 \text{ pc} \left(\frac{n_{\text{H}}}{10^4 \text{ cm}^{-3}} \right)^{-1}, \quad (10)$$

where μ is the mean molecular weight. Equation (10) shows that radiation pressure is effective only to very dense filaments ($n_{\text{H}} \sim 10^4 \text{ cm}^{-3}$) falling within $\sim 1 \text{ pc}$ of a star cluster. Thus the impact of radiation pressure depends on the distribution of the gas and stars. In our simulations, the dense filaments fragment into clumps, which then collapse into stars before reaching $\sim 1 \text{ pc}$ from pre-existing massive stars. This explains why the radiation pressure effect is so weak. Note that the above argument is only applicable for limited cases where the whole cloud collapses nearly spherically owing to relatively weak initial turbulent support. Kim

et al. (2018) showed that with only the radiation pressure feedback the SFE is reduced to ≈ 0.2 assuming $\alpha_0 = 2.0$ instead of our value $\alpha_0 = 0.5$. In such a case, the whole cloud is more violently disrupted by the stronger turbulence and the evolution is no longer approximated with the spherical collapse as in Equation (9).

If $Z \ll 1 Z_{\odot}$, the cloud is not optically thick (see also, sec. 4.2), and the radiation pressure has little impact. Thus, we take only the photoionization feedback into account in developing a semi-analytical model in Section 4.

3.2 Variations among models with different cloud properties

3.2.1 Star formation efficiency

For the models with various M_{cl} , R_{cl} and Z , we obtain the SFE $\epsilon_* \equiv M_*/M_{\text{cl}}$ from the simulations, where M_* is the final total stellar mass. Figure 7 shows the SFE as a function of the initial surface density of the clouds. The SFE increases with the surface density, consistently with previous studies (e.g., Raskutti et al. 2016; Kim et al. 2018; He et al. 2019). For the case with $Z = 1 Z_{\odot}$, the SFE increases from 2 to 30 percent as Σ increases from 8 to 300 $M_{\odot} \text{ pc}^{-2}$. At each metallicity, the SFE is well approximated by a power-law

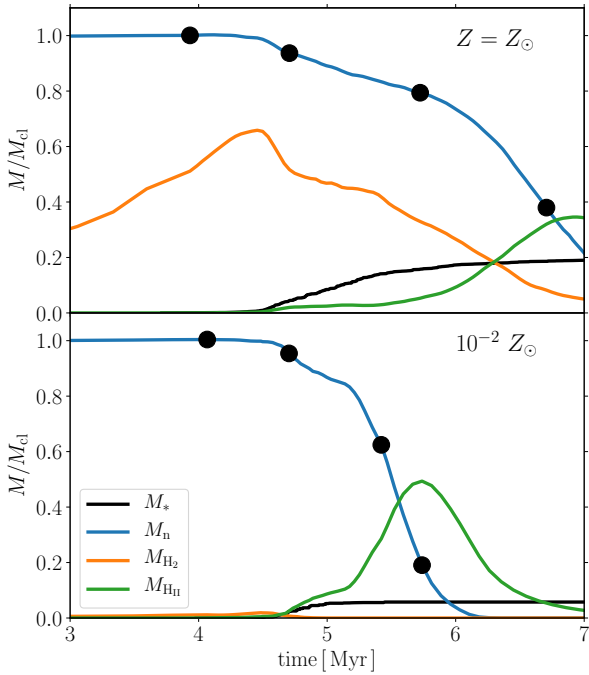


Figure 3. The time evolution of the mass of each component in the cluster-forming clouds with mass $M_{\text{cl}} = 10^5 M_{\odot}$, radius $R_{\text{cl}} = 20 \text{ pc}$, and metallicity $Z = 1 Z_{\odot}$ (top) and $10^{-2} Z_{\odot}$ (bottom). Each line represents the total stellar mass M_* (black), neutral gas mass M_n (blue), H_2 molecule mass M_{H_2} (orange) and ionized gas mass M_{HII} (green). The filled circles mark the four epochs for which we show the snapshots in Figures 1 and 2.

function of the surface density except for the case with the lowest surface density ($\Sigma \sim 8 M_{\odot} \text{pc}^{-2}$).

The SFE also increases with the metallicity. This is because the photoionization feedback that disrupts the star-forming clouds becomes stronger at lower metallicity from the following two reasons. Firstly, the temperature in the HII regions, where the main coolant is the metal lines of OII and OIII (Osterbrock & Ferland 2006), is higher in lower-metallicity cases: its typical value increases from $9 \times 10^3 \text{ K}$ at $Z = 1 Z_{\odot}$ to $2.0 \times 10^4 \text{ K}$ at $Z = 10^{-2} Z_{\odot}$. The resultant higher pressure causes more rapid expansion of the HII regions and thus stronger feedback to the star-forming clouds. Secondly, the ionizing photons are less attenuated by dust grains in lower-metallicity cases. As discussed in Section 3.1, in the case with $Z = 1 Z_{\odot}$, the star-forming filaments can survive even after the HII regions begin to expand because dust grains shield the neutral gas from the photoionization. For the case with $Z = 10^{-2} Z_{\odot}$, however, the filaments are easily photoionized and soon disrupted. From the reasons above, the duration of star formation is short, and thus the SFE is low in lower-metallicity environments. The dust shielding of the filaments will be discussed analytically in Section 4.2.

3.2.2 Lifetime of the clouds

In Figure 8, we show the lifetime of cluster-forming clouds t_{life} as a function of the surface density. In the numerical simulations, we define the cloud lifetime as elapsed time

since the start of the simulations until the total stellar mass reaches 90 percent of the final value. In low surface-density cases with $\Sigma \lesssim 30 M_{\odot} \text{pc}^{-2}$, the duration of the star formation is much shorter than the free-fall time of the clouds, and hence the lifetime is almost equal to the latter. In high surface-density cases with $\Sigma \gtrsim 70 M_{\odot} \text{pc}^{-2}$, however, the lifetime is slightly longer than the free-fall time because of the longer expansion time of the HII regions.

3.3 Evolution of cluster particles

The early evolution of newborn star clusters depends on the initial cloud surface-density and metallicity. In a more compact and higher-metallicity cloud, the SFE and the total stellar mass are higher. Thus the star cluster formed there tends to remain gravitationally bound. In our case, the star clusters remain gravitationally bound until the end of the simulation only in cases with metallicity $Z = 1 Z_{\odot}$ and with initial surface density $\Sigma \gtrsim 80 M_{\odot} \text{pc}^{-2}$. In Figure 9, the time evolution of the half-mass radius of the star clusters formed in our simulations is shown in some cases. In the case with $(M_{\text{cl}}, R_{\text{cl}}, Z) = (10^5 M_{\odot}, 20 \text{ pc}, 1 Z_{\odot})$, where $\Sigma \simeq 80 M_{\odot} \text{pc}^{-2}$, the half-mass radius remains constant at 1.5 pc ($\sim 0.075 R_{\text{cl}}$) after the quenching of the star formation, and the star clusters remain gravitationally bound. We see that even with the same Σ , the clusters finally dissolve at lower metallicities. In other cases with $\Sigma \simeq 32 M_{\odot} \text{pc}^{-2}$, the half-mass radii increase monotonously and the star clusters become unbound regardless of Σ . In these cases, the timescale of dissolving the clusters corresponds to that of the HII-region expansion. Before the disruption of the clouds, the star cluster is trapped in the central region due to the gravitational potential of the gas. However, it becomes shallower after the HII-region expansion and the star cluster comes apart if the gravitational binding is not sufficient, as shown in Figure 9. Although we use the approximate method with which the sink particles also represent clusters with very small mass in our simulations, the above trend may be consistent with the high “infant mortality” of embedded clusters (e.g., Lada & Lada 2003).

In Figure 10, the mass distribution of the cluster particles are shown for cases with metallicities $Z = 1 Z_{\odot}$ and $10^{-2} Z_{\odot}$. We see that the mass spectrum at $Z = 10^{-2} Z_{\odot}$ is much flatter than that at $Z = 1 Z_{\odot}$. The mass distribution at $Z = 1 Z_{\odot}$ is well fitted by a power-law $dN/dM_* \propto M_*^{-2}$, which is consistent with observed mass functions of nearby open and young massive clusters (e.g., Portegies Zwart et al. 2010; Krumholz et al. 2019). We argue that this dependence on metallicity comes from how tight the system is gravitationally bound. In the case with $Z = 10^{-2} Z_{\odot}$, the cluster particles are only loosely bound at birth and immediately dissolve through the cloud dispersal as described above. Mergers between cluster particles hardly occur. We have confirmed that, although not presented, the flat mass distribution is broadly observed in the other cases where the particles become unbound after the cloud dispersal. At $Z = 1 Z_{\odot}$, on the other hand, the cluster particles are more tightly bound for long enough time, resulting in more frequent merger events. It appears that the power-law mass distribution is a result of such difference in the evolution.

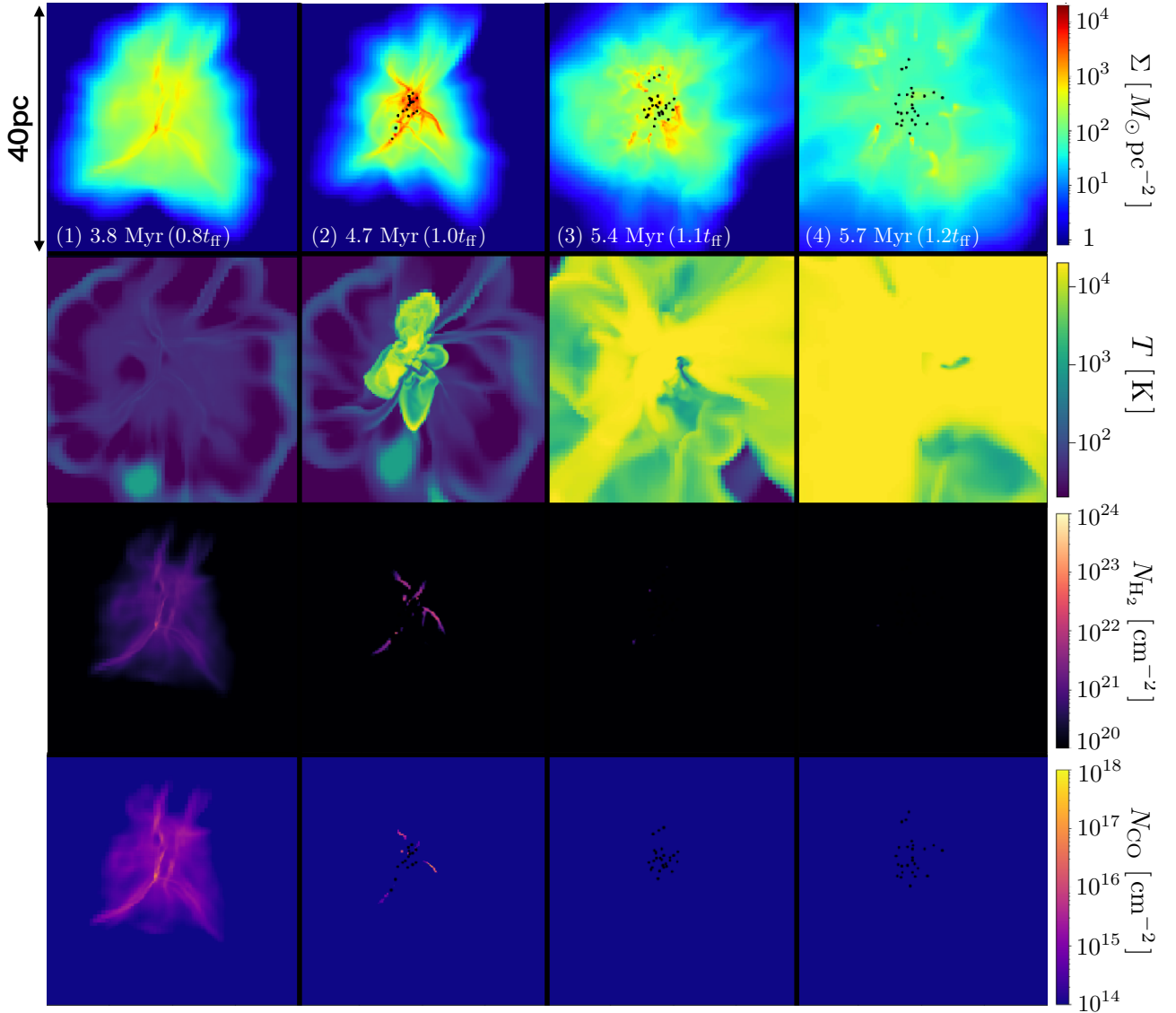


Figure 4. Same as Figure 1, but for the cloud with $(M_{\text{cl}}, R_{\text{cl}}, Z) = (10^5 M_{\odot}, 20 \text{ pc}, 10^{-2} Z_{\odot})$. The color scales for the column densities of H_2 and CO molecules are different from those in Figure 1.

4 SEMI-ANALYTICAL ARGUMENT

4.1 Dependency of SFE on physical conditions of clouds

As shown in the previous section, the SFE and the cloud lifetime vary with the initial surface density and metallicity in our simulations. In previous works, semi-analytical models have been developed to interpret the simulation results, particularly the variation of the SFE. Kim et al. (2018) considered the total momentum of the neutral and ionized gases ejected from photoevaporating clouds, using their simulation results. He et al. (2019) evaluated the SFE using the star formation rate and the sound crossing time of HII regions calibrated with their simulation results, although limited only to the case of $Z = 1 Z_{\odot}$. In this section, we construct a new semi-analytical model in a different approach, paying special attention to the metallicity dependence of photoion-

ization feedback. We consider the propagation time of ionizing front t_{HII} as the duration of star formation because the star formation continues until the expanding HII bubbles terminate gas supply by inflows to dense star-forming regions. Then, the total stellar mass $M_* = \epsilon_* M_{\text{cl}}$ is obtained by multiplying t_{HII} with the star formation rate \dot{M}_* . In our model, t_{HII} also depends on the total stellar mass of radiation sources. Besides, the star formation rate \dot{M}_* varies with metallicity because the cooling time of gas becomes longer in low-metallicity environments. Therefore, we need to calculate the SFEs ϵ_* , the propagation time t_{HII} , and the star formation rate \dot{M}_* consistently. In the following, we consider the conversion rate of the neutral gas to stars in order to formulate the star formation rate \dot{M}_* in Section 4.1.1. We then construct a model for the SFE ϵ_* and the propagation time t_{HII} in Section 4.1.2.

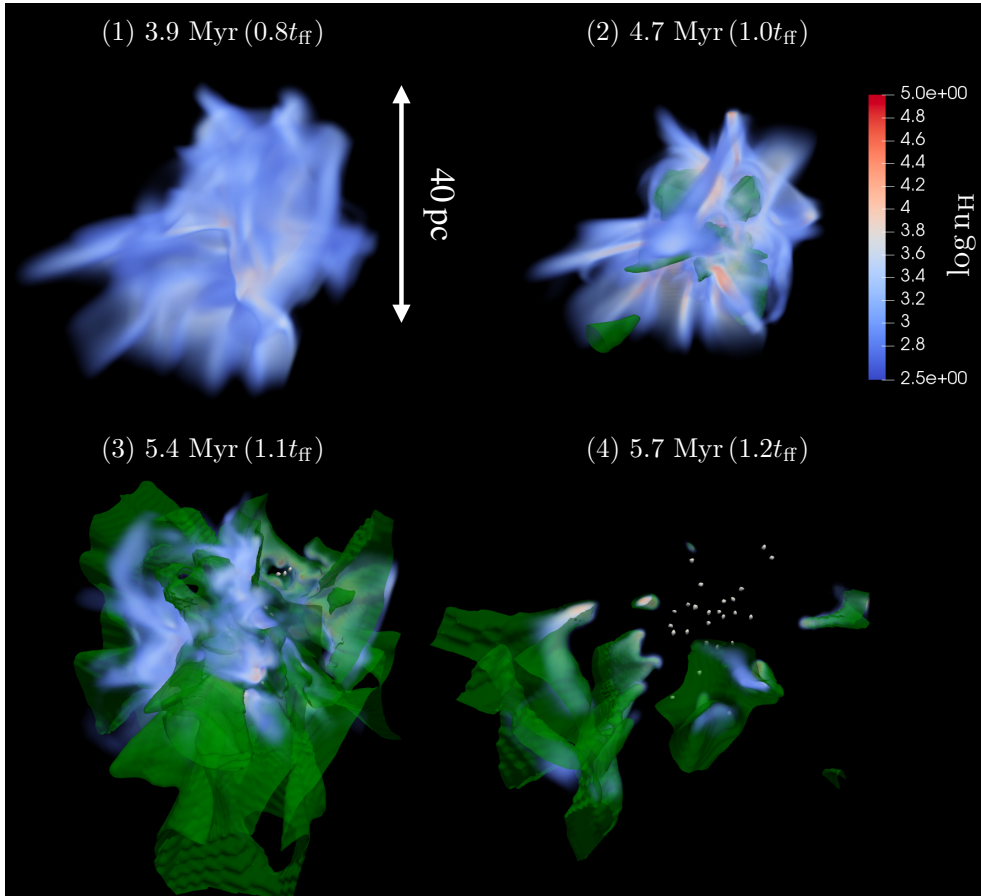


Figure 5. Same as Figure 2, but for the cloud with $(M_{\text{cl}}, R_{\text{cl}}, Z) = (10^5 M_{\odot}, 20 \text{ pc}, 10^{-2} Z_{\odot})$. Each panel shows the snapshot at the same epoch as in Figure 4.

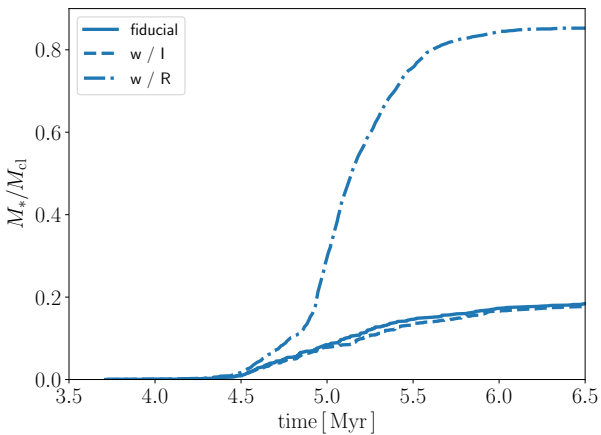


Figure 6. Impact of photoionization and radiation pressure on star formation. Each line shows the time evolution of the total stellar mass in the cloud with $(M_{\text{cl}}, R_{\text{cl}}, Z) = (10^5 M_{\odot}, 20 \text{ pc}, 1 Z_{\odot})$. The solid line represents the fiducial case (M5R20Z0) as shown in Figure 3. Other lines show the cases where we only consider either photoionization (dashed line, M5R20Z0PI) or radiation pressure (dot-dashed line, M5R20Z0RP).

4.1.1 Fraction of star-forming gas around star clusters

We find that only a part of neutral gas around stars is used for the subsequent star formation in our simulations. We thus first estimate the amount of cold gas as a reservoir for the star formation. As shown in Figures 2 and 5, the neutral and ionized regions coexist around star clusters. The neutral gas is vulnerable to compressional heating by the expanding HII bubbles and the feedback by FUV photons is secondary. At $Z = 1 Z_{\odot}$, those dense regions are shielded from EUV/FUV photons by dust grains (see Sec 4.2), and the photodissociation of molecules and photoelectric heating are inefficient. At low-metallicities, on the other hand, UV radiation can penetrate the clouds, but the clouds consist of atomic gas originally, and the dust content is low. Thus, both the photodissociation and photoelectric heating are not important in the neutral gas around the HII regions. Main cooling processes are the dust cooling and line emission of CO, CII and OI. From the thermal balance among these processes, the gas temperature can be higher than a few 100 K, depending on metallicity. With higher temperatures, the collapse of a dense part is delayed until its mass exceeds the higher value of Jeans mass by accreting more surrounding gas. In this case, a warm gas can be evacuated due to photoionization instead of collapse. Only the gas with temperature below the threshold value collapses promptly, resulting in star formation. Here, we assume the critical temperature

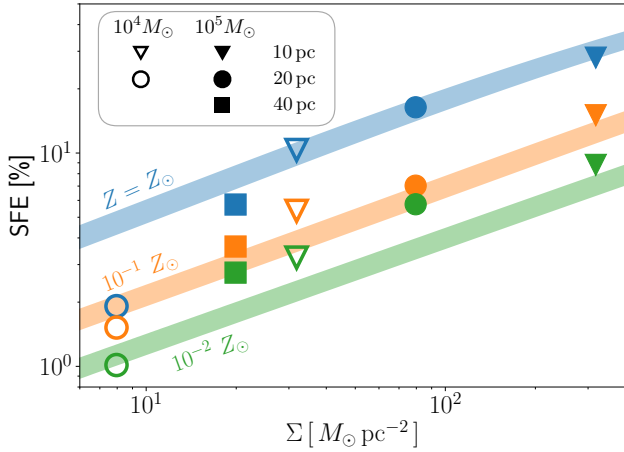


Figure 7. The star formation efficiency (SFE) as a function of the cloud surface density Σ , mass M_{cl} , and metallicity Z . The symbols represent the simulation results for the clouds with the different radii $R_{\text{cl}} = 10$ pc (square), 20 pc (circle), and 40 pc (triangle), and with the different masses $M_{\text{cl}} = 10^5 M_{\odot}$ (filled) and $10^4 M_{\odot}$ (open). The shaded stripes show our analytical estimate of the SFE for the clouds with mass between $M_{\text{cl}} = 10^4$ and $10^5 M_{\odot}$ given by Equation (20). The different colors represent different metallicities of $Z = 1 Z_{\odot}$ (blue), $10^{-1} Z_{\odot}$ (orange) and $10^{-2} Z_{\odot}$ (green) for both the symbols and stripes.

$T_{\text{cr}} = 200$ K above which the gas is supposed to be heated up due to the feedback as described above.

Next, we estimate the amount of star-forming gas. We consider the region inside the active star-forming radius (r_{sf}) defined as the distance between the center of mass and the most distant sink particle. Then we estimate the typical mass fraction of the cold gas during the star formation by calculating the time average weighted with the star formation rate,

$$R_{\text{n}} = \frac{\int_{t_{10}}^{t_{90}} \dot{M}_{*} (M_{\text{n}}/M_{\text{gas}}) dt}{\int_{t_{10}}^{t_{90}} \dot{M}_{*} dt}, \quad (11)$$

where M_{n} and M_{gas} are the cold, i.e., $T < 200$ K, and total gas masses. In Equation (11), t_{10} and t_{90} are, respectively, the times when the total stellar mass reaches 0.1 and 0.9 times the final value. Figure 11 presents R_{n} at given metallicity for different cloud column densities. We here exclude the cases with the lowest $\Sigma < 10 M_{\odot} \text{pc}^{-2}$ (open circles in Fig. 7) in evaluating the mean value as those clouds are disrupted without forming the second sink particle. We can see that R_{n} at given metallicity is almost constant regardless of the surface densities Σ . We find that the mean cold gas fraction $\langle R_{\text{n}} \rangle$ decreases with decreasing metallicity as $\langle R_{\text{n}} \rangle = 0.67, 0.36$ and 0.22 at metallicity of $Z = 1 Z_{\odot}, 10^{-1} Z_{\odot}$ and $10^{-2} Z_{\odot}$, respectively.

Figure 12 shows the gas mass distribution on the number density and temperature plane for the cases with $(M_{\text{cl}}, R_{\text{cl}}) = (10^5 M_{\odot}, 20 \text{ pc})$ at $t = t_{\text{ff}}$ (4.7 Myr). With $Z = 1 Z_{\odot}$, dense star-forming gas with $n_{\text{H}} \gtrsim 10^4 \text{ cm}^{-3}$ has low temperature of $30 \text{ K} < T < 200 \text{ K}$. Most of this component is in the molecular state. At low metallicity of $Z = 10^{-2} Z_{\odot}$, on the other hand, there is few dense and cold gas with $T < 100 \text{ K}$ because of inefficient radiative cooling. Star clus-

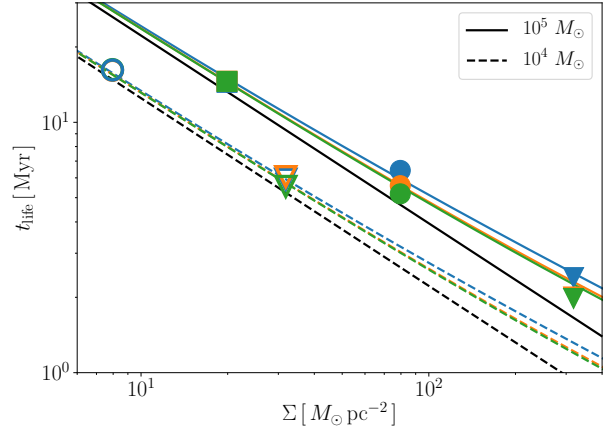


Figure 8. The lifetime of star-forming clouds as a function of the surface density. We use the same symbols and colors as in Figure 7 to indicate the different conditions of $R_{\text{cl}}, M_{\text{cl}}$ and Z . The analytical estimations of the lifetime for the clouds with $M_{\text{cl}} = 10^5 M_{\odot}$ (solid) and $10^4 M_{\odot}$ (dashed) and $Z = 1 Z_{\odot}$ (blue), $10^{-1} Z_{\odot}$ (orange) and $10^{-2} Z_{\odot}$ (green) are also shown with the lines, which are calculated from $t_{\text{life}} = t_{\text{ff}} + t_{\text{HII}}$ with the free-fall time of the clouds t_{ff} (shown with the black lines) and the analytical estimate of the duration of star formation $t_{\text{HII,cl}}$ (Eq. 21).

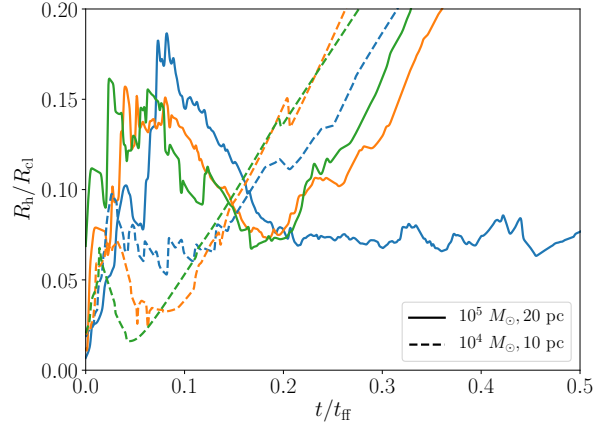


Figure 9. The time evolution of the half-mass radius R_{h} of the cluster particles for the cases with $(M_{\text{cl}}, R_{\text{cl}}) = (10^5 M_{\odot}, 20 \text{ pc})$ (“M5R20” models, solid line) and $(10^4 M_{\odot}, 10 \text{ pc})$ (“M4R10” models, dashed line) as a function of the time normalized by the free fall time of the clouds t_{ff} . The initial surface density Σ is $80 M_{\odot} \text{pc}^{-2}$ for the former cases and $32 M_{\odot} \text{pc}^{-2}$ for the latter. The line colors indicate the metallicity: $Z = 1 Z_{\odot}$ (blue), $10^{-1} Z_{\odot}$ (orange) and $10^{-2} Z_{\odot}$ (green).

ters directly form from such warm and atomic gases. The above features are also highlighted in Figure 13, showing the density-integrated temperature distribution for the same cases. Two peaks at 40-50K and 100K are observable in both cases corresponding to the different main cooling processes, the dust and [CII] cooling, respectively. The lower (higher) temperature peak is higher for $Z = Z_{\odot}$ ($Z = 10^{-2} Z_{\odot}$, respectively). At $Z = 10^{-2} Z_{\odot}$, more neutral gas distributes

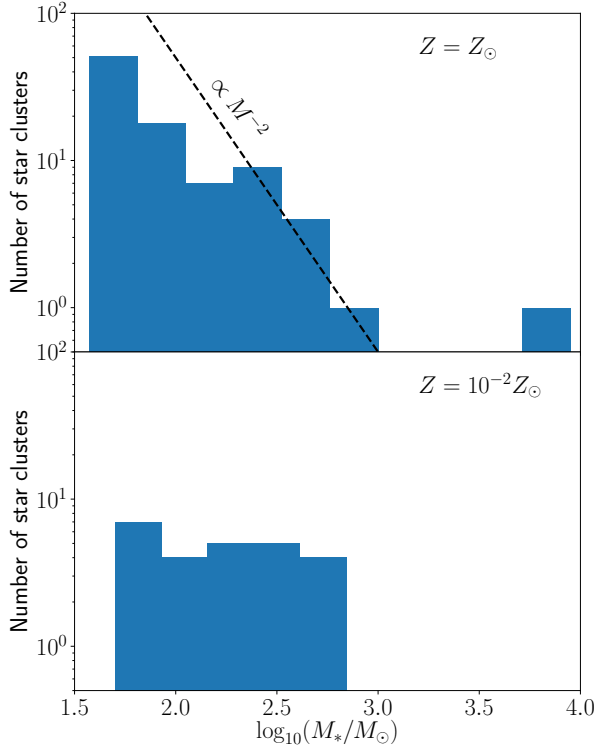


Figure 10. The mass distribution of the cluster particles at the end of the simulations. Top and bottom panels show the cases with $(M_{\text{cl}}, R_{\text{cl}}, Z) = (10^5 M_{\odot}, 20\text{pc}, 1 Z_{\odot})$ and $(10^5 M_{\odot}, 20\text{pc}, 10^{-2} Z_{\odot})$. The dashed line indicates the relation $\propto M_*^{-2}$.

above 10^2 K owing to less efficient [CII] cooling than in the solar metallicity case. In each case, plenty of gas accumulates around the peak temperature because the cooling becomes inefficient below that. Even if the gas is not affected by heating from the newborn stars, it stays at these temperatures for a long time. Thus, we consider the gas with $T < 200$ K as the star-forming gas in both cases.

4.1.2 Star formation efficiencies

Suppose a uniform density sphere whose mass and radius are M_{cl} and R_{cl} . Here we consider dynamics of the boundary shell of the HII region, which encloses the mass $M_{\text{sh}} = M_{\text{cl}} (r_{\text{sh}}/R_{\text{cl}})^3$, where r_{sh} is the radius of the shell. We calculate the motion of the shell driven by the thermal pressure as

$$\frac{d}{dt} (M_{\text{sh}} \dot{r}_{\text{sh}}) = 8\pi k_{\text{B}} T_{\text{i}} n_{\text{i}} r_{\text{sh}}^2 \quad (12)$$

where T_{i} is the temperature of ionized gas (e.g., Matzner 2002; Hosokawa & Inutsuka 2006; Krumholz & Matzner 2009). The number density of the ionization region is given by the balance between the ionization and recombination rates as

$$n_{\text{i}} = \left(\frac{3f_{\text{ion}} S_{\text{ion}}}{4\pi r_{\text{sh}}^3 \alpha_{\text{B}}} \right)^{1/2}, \quad (13)$$

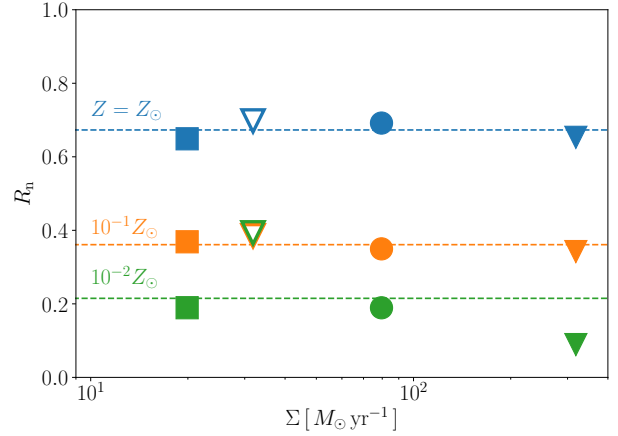


Figure 11. The average fraction of the mass of the cold gas ($T < 200$ K) R_{n} as given in Equation (11). The symbols and colors are same as Figure 7. The dashed lines show the averaged value of R_{n} with $\Sigma > 10 M_{\odot} \text{pc}^{-2}$ (see text) at each metallicity.

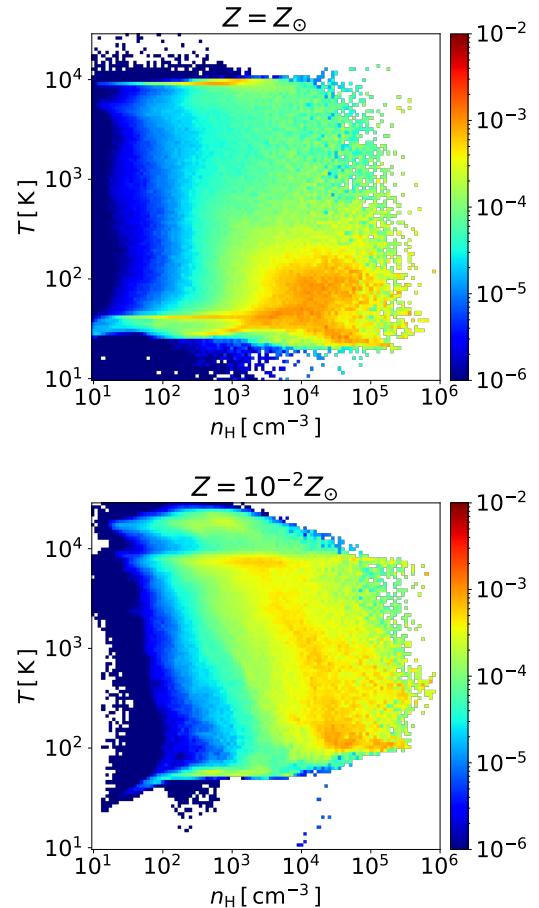


Figure 12. The gas mass distributions on the $n_{\text{H}}-T$ plane within the star-forming region r_{sf} (see text) at the epoch of $t = t_{\text{ff}}$. The top and bottom panels represent the cases with $(M_{\text{cl}}, R_{\text{cl}}, Z) = (10^5 M_{\odot}, 20\text{pc}, 1Z_{\odot})$ and $(10^5 M_{\odot}, 20\text{pc}, 10^{-2} Z_{\odot})$. In each panel the colors show the mass ratio of each bin to the total mass.

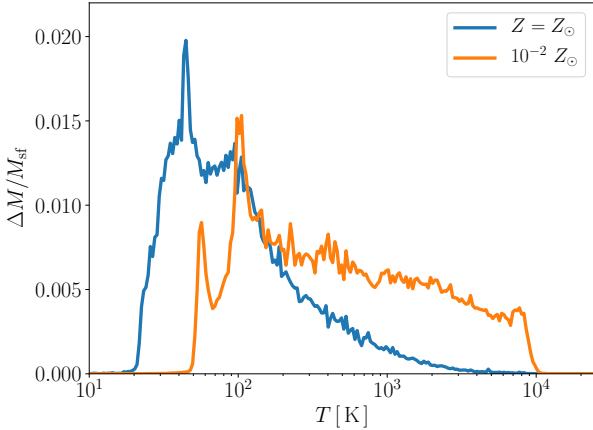


Figure 13. The mass distribution against the temperature within the star-forming region $r < r_{\text{sf}}$ at the epoch of $t = t_{\text{ff}}$. Plotted is the mass fraction at each temperature bin $\Delta M/M_{\text{sf}}$, where M_{sf} is the total mass contained within the radius r_{sf} . Only the non-ionized gas is considered for the plots. The blue and orange lines represent the cases with $(M_{\text{cl}}, R_{\text{cl}}, Z) = (10^5 M_{\odot}, 20\text{pc}, 1Z_{\odot})$ and $(10^5 M_{\odot}, 20\text{pc}, 10^{-2}Z_{\odot})$.

where S_{ion} and α_{B} are the emissivity of ionization photons and the recombination rate coefficient. The emissivity is proportional to the final total mass of sink particles as $S_{\text{ion}} = s_* \epsilon_* M_{\text{cl}}$. The photon production rate per unit mass $s_* = 8.0 \times 10^{46} \text{ s}^{-1} M_{\odot}^{-1}$, calculated from the same isochrone in Section 2.2. The recombination rate coefficient is $\alpha_{\text{B}} = 2.6 \times 10^{-13} (T_i/10^4 \text{ K})^{-0.8} \text{ cm}^3 \text{ s}^{-1}$ (Osterbrock & Ferland 2006). In Equation (13), we introduce the factor f_{ion} that represents the fraction of ionizing photons used for ionization of hydrogen before they are absorbed by dust. We use the fitting function of f_{ion} obtained with the calculation of the hydrostatic structure inside HII regions (Draine 2011). More details of f_{ion} are described in Appendix B. We introduce the following dimensionless parameters,

$$x = r_{\text{sh}}/R_{\text{cl}}, \quad (14)$$

and

$$\tau = \left[\frac{48\pi k_{\text{B}}^2 T_i^2 f_{\text{ion}} s_* \epsilon_*}{\alpha_{\text{B}} M_{\text{cl}} R_{\text{cl}}} \right]^{1/4} t. \quad (15)$$

With these new variables and equation (13), we rewrite equation (12) as

$$\frac{d}{d\tau} \left(x^3 \frac{d}{d\tau} x \right) = x^{1/2}. \quad (16)$$

Equation (16) has the self-similar solution $x = (7\tau/6)^{4/7}$ (Krumholz & Matzner 2009). The ionization front reaches outside the cloud at $x = 1$. By setting $x = 1$, we can derive the propagation time of the ionizing front

$$t_{\text{HII}} = \frac{6}{7} \left[\frac{\alpha_{\text{B}} M_{\text{cl}} R_{\text{cl}}}{48\pi k_{\text{B}}^2 T_i^2 f_{\text{ion}} s_* \epsilon_*} \right]^{1/4}. \quad (17)$$

Here, we have assumed that the emissivity S_{ion} in Equation (13) is given with the final stellar mass. This simple approximation is appropriate because of the weak dependence of the propagation time t_{HII} on the emissivity S_{ion} (Eq. 17).

Assuming the star formation continues until $t \approx t_{\text{HII}}$, we can estimate the total stellar mass M_* as

$$M_* = \epsilon_* M_{\text{cl}} = \dot{M}_* t_{\text{HII}}, \quad (18)$$

where \dot{M}_* is the star formation rate. As the cloud collapses, the gas accretes onto the central dense region at the rate $M_{\text{cl}}/t_{\text{ff}}$ where t_{ff} is the free-fall time of the cloud. However, only a part of the accreted gas is converted into stars due to stellar feedback. Regarding the fraction of cold neutral gas R_{n} (Eq. 11) as the conversion rate to the star clusters, we estimate the star formation rate as

$$\dot{M}_* = R_{\text{n}} \frac{M_{\text{cl}}}{t_{\text{ff}}}, \quad (19)$$

where $t_{\text{ff}} = \sqrt{3\pi/32G\rho}$. The star formation efficiency is estimated from Equation (17), (18) and (19),

$$\epsilon_* = 0.18 \left(\frac{R_{\text{n}}}{0.67} \right)^{4/5} \left(\frac{\Sigma}{80 M_{\odot} \text{pc}^{-2}} \right)^{1/2} \left(\frac{M_{\text{cl}}}{10^5 M_{\odot}} \right)^{1/10} \left(\frac{T_i}{10^4 \text{ K}} \right)^{-14/25} \left(\frac{f_{\text{ion}}}{0.3} \right)^{-1/5}. \quad (20)$$

In Figure 7, the shaded regions represent the SFEs at $M_{\text{cl}} = 10^4$ and $10^5 M_{\odot}$. Here, we use the temperature of ionized gas and the fraction of cold neutral gas $(T_i, R_{\text{n}}) = (9 \times 10^3 \text{ K}, 0.67)$, $(1.6 \times 10^4 \text{ K}, 0.36)$ and $(2 \times 10^4 \text{ K}, 0.22)$ at $Z = 1 Z_{\odot}$, $10^{-1} Z_{\odot}$ and $10^{-2} Z_{\odot}$, respectively, which are obtained from the simulations. Also, f_{ion} is calculated from Equation (B1). Note in the dependency of SFE by Equation (20), the part of $\epsilon_* \propto M_{\text{cl}}^{1/10} \Sigma^{1/2}$ depends on the initial cloud properties and that of $\epsilon_* \propto R_{\text{n}}^{4/5} T_i^{-14/25} f_{\text{ion}}^{-1/5}$ on the metallicity. As can be seen in Figure 7, the semi-analytical model reproduces the simulation results well. At $Z = 1 Z_{\odot}$, the analytical estimate for the model with the lowest- Σ deviates from the numerical simulations because the conversion rate R_{n} decreases, as shown in Figure 11.

Substituting Equation (20) into (17), we can obtain the expansion time of HII regions as

$$t_{\text{HII}} = 1.3 \times 10^6 \text{ yr} \left(\frac{R_{\text{n}}}{0.67} \right)^{-1/5} \left(\frac{\Sigma}{80 M_{\odot} \text{pc}^{-2}} \right)^{-1/4} \left(\frac{M_{\text{cl}}}{10^5 M_{\odot}} \right)^{7/20} \left(\frac{T_i}{10^4 \text{ K}} \right)^{-9/25} \left(\frac{f_{\text{ion}}}{0.3} \right)^{-1/5}. \quad (21)$$

The lifetime of cluster-forming clouds is the sum of the free-fall time and the expansion time of HII regions as $t_{\text{life}} = t_{\text{ff}} + t_{\text{HII}}$. In Figure 8, the solid and dashed lines show the lifetime of cluster-forming clouds estimated with Equation (21). The analytical results coincide with the numerical ones. Because of weaker dependence of t_{HII} on the surface density ($\propto \Sigma^{-1/4}$) compared with $t_{\text{ff}} (\propto \Sigma^{-1/2})$, the lifetime of cluster-forming clouds becomes significantly longer than t_{ff} as Σ increases.

4.2 Conditions of dust shielding

Turbulent motions create sheet-like density fluctuations as shown in Figures 2 and 5. These structures survive even after the HII region expansion in the case of $Z = 1 Z_{\odot}$ (Fig. 2-3) while they completely disappear in the case of $Z = 10^{-2} Z_{\odot}$ (Fig. 5-3). This difference comes from the

fact that the optical depth of such structures against ionizing photons depends on metallicity as the dust grains are the main source of opacity. In the shade of optically-thick sheets, the gas can flow into the star-forming regions, and the star formation continues until the sheets are disrupted by the HII-region expansion. Below we analytically estimate the optical depth of such sheets and clumps, and consider under what conditions such dense structures are protected against UV photons by dust attenuation. This is useful to understand the simulation results because these quantities should be related to the metallicity-dependence of the cold gas mass fraction R_n (Eq. 11), which is higher with higher metallicity.

On large scales, where the turbulence is supersonic, the turbulent velocity field dominates the cloud evolution, and the gas accumulates into the sheet-like structures. Star formation occurs after one free-fall time from the start of the collapse. Until then, large-scale sheets are formed via the gas swept up on the scale where the crossing time $l/\sigma(l)$ is equal to the free fall time t_{ff} :

$$l_c = 7.4 \text{ pc} \left(\frac{R_{\text{cl}}}{20 \text{ pc}} \right) \left(\frac{\alpha_0}{0.5} \right), \quad (22)$$

where we use the scaling relation of velocity dispersion $\sigma(l) \propto l^{1/2}$ (Larson 1981), with the normalization given by $\sigma_0 = (3\alpha_0 GM_{\text{cl}}/5R_{\text{cl}})^{1/2}$ (see Eq. 8). We estimate the optical depth of the sheet to ionizing photons with the cross section of dust grains $\sigma_d = 10^{-21} \text{ cm}^2(Z/Z_\odot)$ as

$$\tau_{\text{sh}} = \sigma_d n_0 l_c = 2.0 \left(\frac{\Sigma}{80 M_\odot \text{ pc}^{-2}} \right) \left(\frac{\alpha_0}{0.5} \right) \left(\frac{Z}{Z_\odot} \right), \quad (23)$$

where n_0 is the mean number density of the cluster-forming cloud. At $Z = 1 Z_\odot$, the sheets are protected by photoionization if the surface density is higher than $80 M_\odot \text{ pc}^{-2}$. In other cases, such as low-surface density or low-metallicity cases, dust attenuation becomes ineffective and the sheets are easily photoionized.

On the small scales, where the turbulent velocity becomes subsonic, the critical scale is estimated by comparing the turbulent velocity and sound speed (McKee & Ostriker 2007),

$$l_s = 0.4 \text{ pc} \left(\frac{\Sigma}{80 M_\odot \text{ pc}^{-2}} \right)^{-1} \left(\frac{\alpha_0}{0.5} \right)^{-1} \left(\frac{T}{20 \text{ K}} \right), \quad (24)$$

where T is the gas temperature. At a scale smaller than l_s , if the gas cools down and starts to collapse, the turbulent motion cannot suppress the collapse. Therefore, we consider l_s as the typical size of star-forming clumps. Given that $\lambda_J = l_s$, the number density becomes

$$n_{\text{sf}} = 1.9 \times 10^4 \text{ cm}^{-3} \left(\frac{\Sigma}{80 M_\odot \text{ pc}^{-2}} \right)^2 \left(\frac{\alpha_0}{0.5} \right)^2 \left(\frac{T}{20 \text{ K}} \right)^{-1}. \quad (25)$$

Same as for Equation (23), optical depth of the star-forming clouds τ_{sf} is estimated with Equation (24) and (25) as

$$\tau_{\text{sf}} = \sigma_d n_{\text{sf}} l_s = 23 \left(\frac{\Sigma}{80 M_\odot \text{ pc}^{-2}} \right) \left(\frac{\alpha_0}{0.5} \right) \left(\frac{Z}{Z_\odot} \right). \quad (26)$$

At $Z = 1 Z_\odot$ the clump is shielded from UV radiation from neighboring stars. If $Z \ll 0.1 Z_\odot$, the star-forming clouds are ionized, resulting in rapid quenching of star formation.

5 SUMMARY & DISCUSSION

We have performed 3D RHD simulations to systematically study the star cluster formation and cloud dispersal in various environments, including very low-metallicity cases. Our simulations include radiative feedback from massive stars, such as photoionization of hydrogen atoms, photoelectric heating, and photodissociation of molecules. We have investigated the cluster-forming clouds with different surface densities and metallicities, $\Sigma = 10 - 300 M_\odot \text{ pc}^{-2}$ and $Z = 10^{-2} - 1 Z_\odot$. We have also developed a semi-analytical model that reproduces well the simulation results, e.g., the dependence of the star formation efficiency (SFE) on the cloud surface density and metallicity. Our findings are summarized as follows:

(i) Overall evolution in the simulation is qualitatively similar among all the examined cases. As a cloud collapses, the initial turbulent velocity field creates the dense gas filaments, which fragment to form stars. As the mass in stars increases, UV radiation from newborn massive stars creates HII bubbles, which expands due to its high thermal pressure and eventually blow away surrounding non-ionized gas. Once the radiative feedback becomes effective, the star formation is quenched within a free-fall time. That is, the natal cloud is promptly disrupted after the massive star formation.

(ii) At each metallicity, the SFE ϵ increases with increasing initial surface density Σ . At $Z = 1 Z_\odot$, for instance, $\epsilon_* = 0.02$ for $\Sigma = 10 M_\odot \text{ pc}^{-2}$ and $\epsilon_* = 0.3$ for $\Sigma = 300 M_\odot \text{ pc}^{-2}$. Those values of a few percent for the clouds with the surface densities $\sim 10 M_\odot \text{ pc}^{-2}$ are consistent with recent observations of GMCs in a nearby galaxy (e.g., Kruijssen et al. 2019).

(iii) At low metallicity, clusters form in atomic clouds as the molecule formation time is longer than the cooling or dynamical time. We have found that the SFE is systematically lower for lower metallicity with the reduction factor $\simeq 0.3$ at $Z = 10^{-2} Z_\odot$, regardless of Σ . In low-metallicity environments, the temperature of the photoionized gas is high due to ineffective radiative cooling and dust attenuation of ionizing photons. This leads to a more rapid expansion of the HII regions, which terminates the star formation over the cloud in a shorter timescale. The newborn clusters are less gravitationally bound after the cloud dispersal than those at the solar metallicity.

(iv) To understand the dependence of SFE on cloud properties and metallicity, we have developed a semi-analytical model that gives SFE agreeing excellently with the simulation results.

CO molecules are the standard tracer of the molecular clouds, i.e., the star-forming cold gas. Since we have consistently solved the thermal and chemical states of the atomic and molecular gas in our simulations, we could follow the time evolution of the CO-to-H₂ conversion factor of the cluster-forming clouds (e.g., Inoguchi et al. 2020), although not focused above. In our simulations for $Z = 1 Z_\odot$, the formation of CO and H₂ molecules occurs in the dense filaments, in which newborn clusters are formed. In the cases of $Z = 10^{-2} Z_\odot$, molecule formation hardly proceeds and the star formation occurs directly from almost atomic gas (Krumholz 2012). Observations suggest a high value of the CO-to-H₂ conversion factor for GMCs with sub-solar metallicity associated with massive star-forming regions (Leroy

et al. 2009). Our simulations should potentially provide such metallicity dependence even for very metal-poor cases with $Z = 10^{-2} Z_{\odot}$, which will be considered in our future studies.

Our simulations show that the cluster formation and cloud dispersal proceed in the filamentary gas. Given that a strong magnetic field exists in the cloud, the gas structure will change significantly (e.g., Inoue & Inutsuka 2012; Inutsuka et al. 2015). Also, the magnetic fields give support to collapsing GMCs and delay the star formation (Geen et al. 2015). We plan to study the impact of magnetic fields combined with the radiative feedback on star formation in GMCs in future work.

ACKNOWLEDGEMENTS

The authors wish to express their cordial thanks to Profs. Masayuki Umemura and Ken Ohsuga for their continual interest, advice and encouragement. This work is financially supported by the Grants-in-Aid for Basic Research by the Ministry of Education, Science and Culture of Japan (TH: 19H01934, KO:25287040, 17H01102, 17H02869). The numerical simulations were performed on the Cray XC50 (Aterui II) at the Center for Computational Astrophysics (CfCA) of National Astronomical Observatory of Japan and the Cray XC40 at Yukawa Institute for Theoretical Physics in Kyoto University

REFERENCES

- Abel T., Wandelt B. D., 2002, *MNRAS*, **330**, L53
- Bakes E. L. O., Tielens A. G. G. M., 1994, *ApJ*, **427**, 822
- Bigiel F., Leroy A., Walter F., Brinks E., de Blok W. J. G., Madore B., Thornley M. D., 2008, *AJ*, **136**, 2846
- Chabrier G., 2003, *PASP*, **115**, 763
- Chen Y., Bressan A., Girardi L., Marigo P., Kong X., Lanza A., 2015, *MNRAS*, **452**, 1068
- Chevance M., et al., 2020, *MNRAS*, **493**, 2872
- Dale J. E., Ercolano B., Bonnell I. A., 2012, *MNRAS*, **427**, 2852
- Draine B. T., 2011, *ApJ*, **732**, 100
- Draine B. T., Bertoldi F., 1996, *ApJ*, **468**, 269
- Faesi C. M., Lada C. J., Forbrich J., 2018, *ApJ*, **857**, 19
- Fall S. M., Krumholz M. R., Matzner C. D., 2010, *ApJ*, **710**, L142
- Federrath C., Banerjee R., Clark P. C., Klessen R. S., 2010, *ApJ*, **713**, 269
- Fukui Y., Kawamura A., 2010, *ARA&A*, **48**, 547
- Fukushima H., Hosokawa T., Chiaki G., Omukai K., Yoshida N., Kuiper R., 2020, arXiv e-prints, p. arXiv:2004.02364
- Geen S., Hennebelle P., Tremblin P., Rosdahl J., 2015, *MNRAS*, **454**, 4484
- Geen S., Soler J. D., Hennebelle P., 2017, *MNRAS*, **471**, 4844
- Glover S. C. O., Clark P. C., 2012a, *MNRAS*, **421**, 9
- Glover S. C. O., Clark P. C., 2012b, *MNRAS*, **421**, 116
- Gong H., Ostriker E. C., 2013, *ApJS*, **204**, 8
- Gong M., Ostriker E. C., Wolfire M. G., 2017, *ApJ*, **843**, 38
- Górski K. M., Hivon E., Banday A. J., Wand elt B. D., Hansen F. K., Reinecke M., Bartelmann M., 2005, *ApJ*, **622**, 759
- Hartmann L., Ballesteros-Paredes J., Bergin E. A., 2001, *ApJ*, **562**, 852
- Hasegawa K., Semelin B., 2013, *MNRAS*, **428**, 154
- He C.-C., Ricotti M., Geen S., 2019, *MNRAS*, **489**, 1880
- He C.-C., Ricotti M., Geen S., 2020, *MNRAS*, **492**, 4858
- Heckman T. M., Armus L., Miley G. K., 1990, *ApJS*, **74**, 833
- Heckman T. M., Alexandroff R. M., Borthakur S., Overzier R., Leitherer C., 2015, *ApJ*, **809**, 147
- Hollenbach D., McKee C. F., 1979, *ApJS*, **41**, 555
- Hollenbach D. J., Tielens A. G. G. M., 1999, *Reviews of Modern Physics*, **71**, 173
- Hosokawa T., Inutsuka S.-i., 2005, *ApJ*, **623**, 917
- Hosokawa T., Inutsuka S.-i., 2006, *ApJ*, **646**, 240
- Hosokawa T., Hirano S., Kuiper R., Yorke H. W., Omukai K., Yoshida N., 2016, *ApJ*, **824**, 119
- Inoguchi M., Hosokawa T., Mineshige S., Kim J.-G., 2020, arXiv e-prints, p. arXiv:2004.04171
- Inoue T., Inutsuka S.-i., 2012, *ApJ*, **759**, 35
- Inutsuka S.-i., Inoue T., Iwasaki K., Hosokawa T., 2015, *A&A*, **580**, A49
- Kennicutt Robert C. J., 1998, *ApJ*, **498**, 541
- Kim J.-G., Kim W.-T., Ostriker E. C., 2016, *ApJ*, **819**, 137
- Kim J.-G., Kim W.-T., Ostriker E. C., 2018, *ApJ*, **859**, 68
- Kim J.-G., Kim W.-T., Ostriker E. C., 2019, *ApJ*, **883**, 102
- Kruijssen J. M. D., et al., 2019, *Nature*, **569**, 519
- Krumholz M. R., 2012, *ApJ*, **759**, 9
- Krumholz M. R., Matzner C. D., 2009, *ApJ*, **703**, 1352
- Krumholz M. R., Matzner C. D., McKee C. F., 2006, *ApJ*, **653**, 361
- Krumholz M. R., McKee C. F., Bland -Hawthorn J., 2019, *ARA&A*, **57**, 227
- Lada C. J., Lada E. A., 2003, *ARA&A*, **41**, 57
- Laor A., Draine B. T., 1993, *ApJ*, **402**, 441
- Larson R. B., 1969, *MNRAS*, **145**, 271
- Larson R. B., 1981, *MNRAS*, **194**, 809
- Lee H. H., Herbst E., Pineau des Forets G., Roueff E., Le Bourlot J., 1996, *A&A*, **311**, 690
- Leroy A. K., et al., 2009, *ApJ*, **702**, 352
- Madau P., Dickinson M., 2014, *ARA&A*, **52**, 415
- Mathis J. S., Rumpl W., Nordsieck K. H., 1977, *ApJ*, **217**, 425
- Matsumoto T., 2007, *PASJ*, **59**, 905
- Matsumoto T., Dobashi K., Shimoikura T., 2015, *ApJ*, **801**, 77
- Matzner C. D., 2002, *ApJ*, **566**, 302
- McKee C. F., Ostriker E. C., 2007, *ARA&A*, **45**, 565
- Momose R., et al., 2013, *ApJ*, **772**, L13
- Murray N., Quataert E., Thompson T. A., 2010, *ApJ*, **709**, 191
- Nakatani R., Hosokawa T., Yoshida N., Nomura H., Kuiper R., 2018, *ApJ*, **857**, 57
- Nelson R. P., Langer W. D., 1997, *ApJ*, **482**, 796
- Omukai K., Nishi R., 1998, *ApJ*, **508**, 141
- Omukai K., Tsuribe T., Schneider R., Ferrara A., 2005, *ApJ*, **626**, 627
- Omukai K., Hosokawa T., Yoshida N., 2010, *ApJ*, **722**, 1793
- Osterbrock D. E., Ferland G. J., 2006, *Astrophysics of gaseous nebulae and active galactic nuclei*
- Penston M. V., 1969, *MNRAS*, **144**, 425
- Pillepich A., et al., 2018, *MNRAS*, **475**, 648
- Portegies Zwart S. F., McMillan S. L. W., Gieles M., 2010, *ARA&A*, **48**, 431
- Raskutti S., Ostriker E. C., Skinner M. A., 2016, *ApJ*, **829**, 130
- Rosdahl J., Blaizot J., Aubert D., Stranex T., Teyssier R., 2013, *MNRAS*, **436**, 2188
- Schaye J., et al., 2010, *MNRAS*, **402**, 1536
- Sugimura K., Matsumoto T., Hosokawa T., Hirano S., Omukai K., 2020, *ApJ*, **892**, L14
- Vázquez-Semadeni E., Colín P., Gómez G. C., Ballesteros-Paredes J., Watson A. W., 2010, *ApJ*, **715**, 1302
- Williams J. P., McKee C. F., 1997, *ApJ*, **476**, 166
- Wise J. H., Turk M. J., Norman M. L., Abel T., 2012, *ApJ*, **745**, 50
- Wolfire M. G., Cassinelli J. P., 1987, *ApJ*, **319**, 850
- Yajima H., Nagamine K., Zhu Q., Khochfar S., Dalla Vecchia C., 2017, *ApJ*, **846**, 30

APPENDIX A: RADIATIVE PROCESS

As discussed in Section 2.1, we use the adoptive ray-tracing method for radiation transfer (Abel & Wandelt 2002). In this method, we calculate the equation of radiation transfer from each radiation source, discretizing the solid angle with HEALPix (Górski et al. 2005). In the regions far from the radiation sources, we split the ray to ensure that three rays always cross each cell.

In raytracing, we calculate the column densities of atomic hydrogen N_{HI} , hydrogen atom N_{Hn} , H_2 and CO (N_{H_2} , N_{CO}). The EUV radiation energy flux is calculated as

$$F_{\text{EUV}} = \frac{L_{*,\text{EUV}}}{4\pi r^2} \exp[-(\sigma_{\text{HI}}N_{\text{HI}} + \sigma_{\text{d}}N_{\text{Hn}})], \quad (\text{A1})$$

where $L_{*,\text{EUV}}$ is the EUV luminosity of each radiation source. To obtain the cross-sections of atomic hydrogen and dust grains, we pre-calculate the frequency averaged cross-section with the energy spectrum of radiation sources in the frequency range $13.6 \text{ eV} \leq h\nu \leq 10^3 \text{ eV}$. We use the approximation formula of the cross-section for hydrogen atoms as $\sigma_{\text{HI}}(\nu) = 6.3 \times 10^{-18} (\nu/\nu_{\text{L}})^{-3} \text{ cm}^2$ (Osterbrock & Ferland 2006) where ν_{L} is the Lyman limit frequency. The cross-sections of dust grains are given by Laor & Draine (1993), assuming that the dust-to-gas mass ratio is 0.01 at $Z = 1 Z_{\odot}$. We consider only the dust attenuation for the FUV light and the continuum components as

$$F_i = \frac{L_{*,i}}{4\pi r^2} \exp[-\sigma_{\text{d},i}N_{\text{Hn}}] \quad (i = \text{FUV, continuum}), \quad (\text{A2})$$

where σ_i is the frequency averaged cross section in the frequency range $11.2\text{eV} \leq h\nu \leq 13.6 \text{ eV}$ ($h\nu \leq 11.2\text{eV}$) for FUV photons (continuum components, respectively). We include the radiation force caused by absorption on dust grains and neutral hydrogen at the three components of the radiation field in the hydrodynamics calculations. Note that, in our simulations, the radiation force is secondary compared to the photo-ionization heating.

In chemical and thermal solvers, we consider photoionization (HI and OII), photodissociation (H_2 , and CO), photoelectric heating and dust heating as follows.

The photoionization rates for HI and OII is obtained as

$$R_{\text{HI}} = \int_{\nu_{\text{I}}}^{\infty} d\nu \sigma_{\text{HI}}(\nu) \frac{F_{\nu}}{h\nu}, \quad (\text{A3})$$

$$R_{\text{OII}} = \int_{\nu_{\text{OII}}}^{\infty} d\nu \sigma_{\text{OII}}(\nu) \frac{F_{\nu}}{h\nu}, \quad (\text{A4})$$

where ν_{I} and ν_{OII} are the ionization limit frequency for HI and OII. Here, we use the cross section of HI (σ_{HI}) and OII (σ_{OII}) of Osterbrock & Ferland (2006).

We use the H_2 photodissociation rate of Draine & Bertoldi (1996) as Fukushima et al. (2020), considering dust absorption and self-shielding. We estimate the photodissociation rate of CO and the photoelectric heating rate with the same method of Nakatani et al. (2018). The photodissociation rate of CO molecules is given as (Lee et al. 1996)

$$R_{\text{CO}} = G_{\text{FUV}} p_{\text{diss}} n_{\text{CO}} \Theta_1(N_{\text{CO}}) \Theta_2(N_{\text{H}_2}) \Theta_3(A_{\text{V}}), \quad (\text{A5})$$

where n_{CO} , $A_{\text{V}} = 5.3 \times 10^{-22} N_{\text{Hn}}(Z/Z_{\odot})$ and $p_{\text{diss}} = 1.03 \times 10^{-10} \text{ s}^{-1}$ are the number density of CO, the visual extinction and the unshielded CO photodissociation rate. The strength of FUV is represented with the averaged interstellar flux

$F_{\text{ISRF}} = 1.6 \times 10^{-3} \text{ erg cm}^{-2} \text{ s}^{-1}$ as $G_{\text{FUV}} = L_{\text{FUV}}/(4\pi r^2 F_{\text{ISRF}})$ where L_{FUV} is the FUV luminosity. The rates of self-shielding, H_2 shielding, and dust shielding (Θ_1 , Θ_2 and Θ_3) are given in Tables of Lee et al. (1996).

We use the analytical formula of Bakes & Tielens (1994) for the photoelectric heating as

$$\Gamma_{\text{pe}} = 10^{-24} \epsilon_{\text{pe}} n_{\text{H}} G_{\text{FUV}} \exp(-1.8A_{\text{V}}) \left(\frac{Z}{Z_{\odot}} \right), \quad (\text{A6})$$

where the exponential factor represents the dust absorption (Nakatani et al. 2018), and ϵ_{pe} is given with G_{FUV} and the number density of electron as

$$\epsilon_{\text{pe}} = \frac{4.87 \times 10^{-2}}{1 + 4 \times 10^{-3} \gamma_{\text{pe}}^{0.73}} + \frac{3.65 \times 10^{-2} (T/10^4)^{0.7}}{1 + 2 \times 10^{-4} \gamma_{\text{pe}}}, \quad (\text{A7})$$

where $\gamma_{\text{pe}} = G_{\text{FUV}} \exp(-1.8A_{\text{V}}) \sqrt{T}/n_{\text{e}}$.

To obtain the dust temperature, we calculate the balance among the dust thermal emission, absorption of the direct light (EUV, FUV and continuum), and energy transport from gases. We use the energy transport rate between dust grains and gases given by Hollenbach & McKee (1979). Further details are shown in Fukushima et al. (2020).

APPENDIX B: HYDROGEN ABSORPTION FRACTION OF IONIZING PHOTONS

In Section 4.1.2, we use the fitting formula of Draine (2011) for a fraction of EUV photons absorbed by hydrogen atoms in HII regions. Draine (2011) construct the model of the hydrostatic structure of HII regions, including the thermal pressure and radiation pressure induced by photoionization and dust grains. When radiation pressure becomes strong enough, the shell structure is formed inside the HII regions and the recombination of hydrogen is enhanced due to the high density of the shell. We incorporate these dynamical effects for f_{ion} , although the constant density is assumed in HII regions in our semi-analytical model. The fraction of hydrogen ionization for EUV photons f_{ion} is given as

$$f_{\text{ion}} = \frac{1}{1 + (2/3 + AB)\tau_{\text{d},0}} + \frac{AB\tau_{\text{d},0}}{1 + B\tau_{\text{d},0}}, \quad (\text{B1})$$

where $\tau_{\text{d},0}$ is the optical depth of HII region as

$$\tau_{\text{d},0} = 2.1 \left(\frac{\sigma_{\text{d}}}{10^{-21} \text{ cm}^{-2}} \right) \left[\left(\frac{S_{\text{ion}}}{10^{49} \text{ s}^{-1}} \right) \left(\frac{n_{\text{i}}}{10^3 \text{ cm}^{-3}} \right) \right]^{1/3} \left(\frac{T_{\text{i}}}{10^4 \text{ K}} \right)^{0.28}. \quad (\text{B2})$$

In Equation (B2), S_{ion} , n_{i} and T_{i} are the emissivity of ionizing photons, the number density and the temperature in the HII regions. Here, we use the cross section of dust grains as $\sigma_{\text{d}} = 10^{-21} \text{ cm}^{-2} (Z/Z_{\odot})$. In the original formula of Draine (2011), they use the root mean square of the number density in Equation (B2). It is not significantly different from the uniform density n_{i} in our parameter setups. The parameters of A and B are given as

$$A = \frac{1}{1 + 0.75\gamma^{0.65}\beta^{-0.44}}, \quad (\text{B3})$$

$$B = \frac{0.5}{1 + 0.1(\gamma/\beta)^{1.5}}, \quad (\text{B4})$$

where β and γ are determined by the luminosity ratio of ionizing and non-ionizing radiation (L_n, L_i) and the temperature of HII regions as

$$\beta = \frac{L_n}{L_i}, \quad (\text{B5})$$

$$\gamma = 11.2 \left(\frac{T_i}{10^4 \text{ K}} \right)^{1.83} \left(\frac{18 \text{ eV}}{\langle h\nu \rangle} \right) \left(\frac{\sigma_d}{10^{-21} \text{ cm}^{-2}} \right), \quad (\text{B6})$$

In Equation (B6), we assume that the average energy of ionizing photons becomes $\langle h\nu \rangle = 18 \text{ eV}$, which is the typical one for the stellar IMF, metallicity and age in our simulations.

This paper has been typeset from a $\text{\TeX}/\text{\LaTeX}$ file prepared by the author.